



# Composition-engineered FeCo nanoalloys with lattice expansion and optimized electron structure boosting electrocatalytic Nitrate reduction

Yang Liu<sup>a</sup>, Xiu Zhong<sup>a</sup>, Mengting Liu<sup>a</sup>, Hongyao Zhao<sup>a</sup>, Zhenxiao Wang<sup>a</sup>, Ruiting Ni<sup>a</sup>, Yanyun Wang<sup>a</sup>, Jun Yang<sup>b</sup>, Fei Gao<sup>a</sup>, Yingguo Li<sup>a</sup>, Enxian Yuan<sup>c,\*</sup>, Aihua Yuan<sup>a</sup>, Weidong Shi<sup>a,\*</sup>, Fu Yang<sup>a,\*</sup>

<sup>a</sup> School of Environmental and Chemical Engineering, Jiangsu University of Science and Technology, Zhenjiang, Jiangsu 212003, PR China

<sup>b</sup> School of Material Science & Engineering, Jiangsu University of Science and Technology, Zhenjiang 212003, PR China

<sup>c</sup> School of Chemistry and Chemical Engineering, Yangzhou University, Yangzhou 225002, PR China

## ARTICLE INFO

### Keywords:

Composition engineering  
FeCo alloys  
Electrospinning  
NO<sub>3</sub>RR  
Bimetallic synergy  
Lattice expansion

## ABSTRACT

Herein, composition-engineered CoFe nanoalloys were in-situ constructed and confined in porous fibrous carbon by electrospinning and controlled graphitization, resulting in (110) lattice space expansion and improved free-electron-migration in nanoalloys, delivering bimetallic synergy by electron structural optimization. Impressively, the reinforced NO<sub>3</sub> adsorption and rapid desorption of NH<sub>3</sub> over composition-engineered nanoalloys efficiently promote the electrocatalytic dynamic behavior. As a result, the optimal Co<sub>1</sub>Fe<sub>1.5</sub>/C affords an excellent NH<sub>3</sub> yield of  $48.2 \pm 1.2 \text{ mg h}^{-1} \text{ mg}_{\text{cat}}^{-1}$  and a maximum Faraday efficiency of  $90.8 \pm 1.5 \%$  at  $-1.1 \text{ V}$  vs. RHE, with outstanding stability during 200 h NO<sub>3</sub>RR, outperforming the most state-to-the-art catalysts. An excellent conversion of Nitrate ( $96.4 \pm 0.8 \%$ ) with a high selectivity for Ammonia ( $94.4 \pm 1.2 \%$ ) can be validated. Detailed characterizations including in-situ XPS technique and theoretical calculation studies have demonstrated that Fe composition engineering reinforces the surface adsorption of NO<sub>3</sub>, induces the surface electron redistribution of Co center, and optimizes the reaction pathways, resulting in the remarkable bimetallic synergy and enhancing the surface adsorption of a key intermediate of \*NO over Co sites during the NO<sub>3</sub>RR. Finally, the Zn-NO<sub>3</sub> battery assembled by Co<sub>1</sub>Fe<sub>1.5</sub>/C was explored, which further indicates the potential of Co<sub>1</sub>Fe<sub>1.5</sub>/C in the energy conversion device.

## 1. Introduction

Ammonia (NH<sub>3</sub>) widely not only works as an indispensable presence in agriculture but also is a promising and renewable carbon-free clean energy, belonging to the category of "Green Hydrogen" [1,2]. However, the production of industrial Ammonia from the traditional Haber-Bosch process often causes huge energy depletion and serious environmental threats [3,4]. Therefore, the generation of valuable Ammonia by photo/electrochemical catalyzed reduction of nitrogen or Nitrate under ambient conditions attracts wide research interest [5–7]. Although it is significant to generate NH<sub>3</sub> from nitrogen (N<sub>2</sub>) by electrocatalytic nitrogen reduction reaction (NRR), poor N<sub>2</sub> solubility, high N≡N bonding energy, and sluggish kinetic process result in low NH<sub>3</sub> yields and Faraday efficiencies (FE) [8,9]. Electrocatalytic Nitrate reduction reaction (NO<sub>3</sub>RR) is considered a prospective and alternative way to afford

NH<sub>3</sub> because of the lower bond energies of the N=O bond and the higher solubility of Nitrate in water solution [10,11]. In addition, electrochemical NO<sub>3</sub>RR from various industrial wastewater and municipal sewage discharges can efficiently remove polluted Nitrate and obtain high-value-added chemical products, affording a popular approach for Nitrate-involving wastewater treatment and clean energy regeneration [12–14].

Transition metals (TM) have been widely considered in the design of various catalysts owing to their wide distribution, lower cost, and unsaturated d-orbitals, which are capable of inducing a rearrangement between electrons occurring between the adsorbed molecules and the catalysts, leading to orbitals hybridization with the reactants and following activation [15,16]. Until now, most of the catalysts that were reported for NO<sub>3</sub>RR are popular by using transition metal as the dominant catalytic center. In particular, cobalt (Co)-based catalysts are

\* Corresponding authors.

E-mail addresses: [exyuan@yzu.edu.cn](mailto:exyuan@yzu.edu.cn) (E. Yuan), [swd1978@ujs.edu.cn](mailto:swd1978@ujs.edu.cn) (W. Shi), [fuyang@just.edu.cn](mailto:fuyang@just.edu.cn) (F. Yang).

<https://doi.org/10.1016/j.apcatb.2024.124205>

Received 7 March 2024; Received in revised form 29 April 2024; Accepted 14 May 2024

Available online 16 May 2024

0926-3373/© 2024 Elsevier B.V. All rights are reserved, including those for text and data mining, AI training, and similar technologies.

promising and widely implemented in NO<sub>3</sub>RR [17,18]. In general, Co has a low energy barrier for the dissociation step of NO<sub>2</sub>\* and NO\*, which promotes the desorption of NO<sub>3</sub> and its intermediates and thus accelerates the subsequent hydrogenation step. However, the fast hydrogenation rate of NH<sub>x</sub>\* may be realized at more negative applied potentials (>-0.7 V), which tends to result in higher selectivity for NH<sub>3</sub> synthesis but lower NO<sub>3</sub> reducing activity on Co at too high negative potentials [19]. It may be due to the fact that at high potentials, easily leads to hydrogen evolution competition reactions (HER) over Co catalysts and reduced yield. [20]. Therefore, the achievement of a high NH<sub>3</sub> yield in the NO<sub>3</sub>RR process based on cobalt catalysts is still challenged at a high reaction potential [17,21]. To address above these challenges, some strategies such as interfacial engineering effect [21,22], and electronic structure adjustment [23–25] in the heterogeneous catalyst are usually employed to enhance the intrinsic activity of Co and inhibit the HER during the NO<sub>3</sub>RR. Another approach by coupling bimetallics affords an alternative tactic to optimize the NO<sub>3</sub>RR by relay catalytic process, in particular, the bimetallic active centers could selectively activate the various reaction intermediates to trigger relay catalysis [19,21]. It has been reported that the addition of nickel into Co<sub>3</sub>O<sub>4</sub> improves the electrocatalytic NO<sub>3</sub>RR activity [20], with 94.9 % of Faraday efficiency and 20 mg h<sup>-1</sup> cm<sup>-2</sup> of NH<sub>3</sub> yield at -1.0 V, where the origin of activity enhancement is attributed to the promotion of Co<sub>2</sub>Ni<sub>1-y</sub>(OH)<sub>2</sub> phase for the formation of \*NOH intermediates and inhibiting HER competition. In addition, Sun et al. [26] showed that Pd-doped Co<sub>3</sub>O<sub>4</sub> nano-arrays, improved the adsorption properties of Pd-Co<sub>3</sub>O<sub>4</sub> and optimized the free energy of the intermediates. It resulted in an excellent selectivity for Ammonia with Faraday efficiency of up to 98.7 %. Inspired by the above studies, enzyme-like iron (Fe) in the biological fixation of nitrogen on top of Co-based catalysts is generally demonstrated to easily adsorb NO<sub>3</sub> and possibly afford an interesting coupling effect to synergetically improve the catalytic performance of NO<sub>3</sub>RR. In particular, during the electrocatalytic process, Fe was not only able to lower the dissociation barriers of NO<sub>x</sub>\* [19] but also Fe was able to inhibit the formation of Fe-H bonds, which can inhibit the effects of HER competition reaction, in turn, which benefits to the dominant formation of \*NH bonds during the NO<sub>3</sub>RR, thus increasing the activity of NO<sub>3</sub>RR [11]. Secondly, differing from the conductivity-poor metal oxide catalysts, the alloying bimetal catalyst is an effective strategy to improve the NO<sub>3</sub>RR activity of active metal species by improving the electron transfer and interaction of NO<sub>3</sub>RR. More importantly, constructing the bimetallic synergistic effect of nanoalloys, along with the composition control [27–29] can regulate the asymmetric electronic structure of the metal and optimize the inherent activity of the catalyst in NO<sub>3</sub>RR. In particular, the redistribution of the electronic structure by bimetallic coupling can enhance the intermediate adsorption of NO<sub>3</sub>RR, leading to superior activity and selectivity for electrocatalytic NO<sub>3</sub> reduction than their mono metal. Hu et al. [30] showed that P-doped phosphorus 3D NiFe<sub>2</sub>O<sub>4</sub> not only changed the electronic structure of the catalyst but also induced the charge density and mediated the surface charge state. This bimetallic oxide has higher electrical conductivity and stability compared to monometallic oxides.

However, to our best knowledge, tailored nanoalloys with ultrafine size easily suffer from deactivation during the electrochemical process without any protection. Therefore, the encapsulation of nanoalloys into support is significant to preserving the sustainable electrocatalytic activity. Wang et al. [31] designed a CuBDC@Ti<sub>3</sub>C<sub>2</sub>T<sub>x</sub> two-dimensional flexible electrode. The two-dimensional flexible membrane structure stabilized the Cu sites on the surface and increased the exposed area of catalyst activity, achieving outstanding electrocatalytic activity as well as high cycling stability. Porous carbon can work as promising electrocatalytic active support for accommodating active metal species [32], however, the distribution and regulation of nanoalloys confined into porous carbon to deliver highly-desirable NO<sub>3</sub>RR performance remains rare and unexplored. An interesting phenomenon was demonstrated in our previous work that the introduction of Fe precursor in the

electrospinning process not only contributes to an efficient catalytic active center but also causes the construction of abundant porosity where Fe could work as an activator in the porous activated carbon [16]. Porous carbon fiber support not only works as a protection structure but also accommodates the refined nanoalloys by tandem configuration, thereby improving the electron transfer of various active metal species [27,28]. Such a function could improve the electron transfer process of the catalyst and benefit the adsorption of NO<sub>3</sub> over the catalyst by exposing more active metal sites in the confined porous carbon micro-environment [22,25].

Inspired by the above thoughts, we have constructed porous graphitic carbon loaded CoFe alloyed nanofibers (CoFe/C) by electrospinning technique and controlled graphitized procedure for the first time with flexible Co/Fe ratio for Nitrate reduction reaction (NO<sub>3</sub>RR). Porous structural properties were efficiently regulated by controlled Fe precursor introduction. Electron transfer ability was further optimized when the catalyst was endowed with a rational FeCo ratio, obviously outperforming the monometallic counterparts. More importantly, several unique advantages resulting from the synergistic catalytic effect of CoFe alloying have been demonstrated. First, the alloying of CoFe can optimize the electronic structure of Co, and make the center of Co positively charged, thus enhancing the surface adsorption of intermediates such as \*NO<sub>3</sub>, \*NO<sub>2</sub>, \*NO, and \*NH<sub>2</sub>. In addition, the addition of Fe in an appropriate ratio can significantly inhibit the formation of metal-hydrogen (M-H) bonds on the surface of the catalyst, minimize the competitive reaction and charge consumption of HER, and ensure the efficient hydrogenation reaction of Nitrate and the corresponding intermediates. The optimized Co center dominantly determined the adsorption of key intermediate NO, which synergizes with Fe to improve the NO<sub>3</sub>RR performance. The regulated Fe introduction reinforces the adsorption of NO<sub>3</sub>, which could cause a higher localized reaction concentration and improve the reaction dynamic behavior. The final results showed that the optimally proportioned CoFe alloy catalyst afforded obvious electrocatalytic activity with an Ammonia yield of 48.2 ± 1.2 mg h<sup>-1</sup> mg<sub>cat</sub><sup>-1</sup> and Faraday efficiency (FE) of 90.8 ± 1.5 %, with persistent cycle stability near 200 h. The Zn-NO<sub>3</sub> battery assembled by Co<sub>1</sub>Fe<sub>1.5</sub>/C reaches a high power of 13.7 mW cm<sup>-2</sup> at 0.4 V and achieves a higher NH<sub>3</sub> yield of 72.1 μmol h<sup>-1</sup> cm<sup>-2</sup> at 15 mA cm<sup>-2</sup> and maximum Faraday efficiency of 65.4 % at 6 mA cm<sup>-2</sup>, which further indicates the potential of Co<sub>1</sub>Fe<sub>1.5</sub>/C in the energy conversion.

## 2. Experimental section

### 2.1. Chemicals and materials

Iron(III) acetylacetonate (Fe(C<sub>5</sub>H<sub>7</sub>O<sub>2</sub>)<sub>3</sub> 99 %), Cobalt(II) acetylacetonate (Co(C<sub>5</sub>H<sub>7</sub>O<sub>2</sub>)<sub>2</sub> 99 %), Sodium nitroferricyanide dihydrate (C<sub>5</sub>FeN<sub>6</sub>Na<sub>2</sub>O·2H<sub>2</sub>O 98 %), N, N-Dimethylformamide (C<sub>3</sub>H<sub>7</sub>NO/ DMF 99.8 %), Trisodium citrate dihydrate (Na<sub>3</sub>C<sub>6</sub>H<sub>5</sub>O<sub>7</sub>·2H<sub>2</sub>O 98 %), Phosphoric acid (H<sub>3</sub>PO<sub>4</sub> 85 wt %), Sulfamic acid (H<sub>3</sub>NO<sub>3</sub>S 99 %), N-(1-naphthyl)ethylenediamine dihydrochloride (C<sub>12</sub>H<sub>14</sub>N<sub>2</sub>·2HCl 98 %), p-aminobenzenesulfonamide (C<sub>6</sub>H<sub>8</sub>N<sub>2</sub>O<sub>2</sub>S 99 %), 4-Dimethylaminobenzaldehyde (p-C<sub>9</sub>H<sub>11</sub>NO 99 %), Salicylic acid (C<sub>7</sub>H<sub>6</sub>O<sub>3</sub> 99 %) and Ethanol absolute (C<sub>2</sub>H<sub>5</sub>OH 99.5 %) were ordered from Energy Chemical. Polyacrylonitrile ((C<sub>3</sub>H<sub>3</sub>N)n/ PAN 150 K) and Potassium sulphate (K<sub>2</sub>SO<sub>4</sub> 98 %) were ordered from Macklin Chemical. Hydrazine hydrate (N<sub>2</sub>H<sub>4</sub>·H<sub>2</sub>O AR), 5 wt % Nafion solution, hydrochloric acid (HCl 38 wt %) Sodium, and Hypochlorite (NaClO AR) were ordered from Bidepharm. All reagents were ready to use without further purification.

### 2.2. Synthesis of CoFe/C catalysts

The catalyst can be constructed by electrospun approach and precise graphitization treatment by adjusting the Fe/Co precursor ratios. Firstly, 10 mL DMF bearing 1 mmol of Co(C<sub>5</sub>H<sub>7</sub>O<sub>2</sub>)<sub>2</sub> was introduced to a glass vial with stirring until complete dissolution and then followed by the

addition of 1.5 mmol  $\text{Fe}(\text{C}_5\text{H}_7\text{O}_2)_3$  to reach a transparent state. Afterward, PAN (1.0 g) was poured and stirred for 10 hours to obtain the precursor solution. A syringe was used to extract 10 mL of spinning liquid, the flow rate was controlled at  $50 \mu\text{m min}^{-1}$ , and the distance between the syringe and cylinder was controlled at 15 cm for electrospinning at 18 kV and relative humidity <25 %. The obtained precursor fibers were pre-treated in a vacuum drying oven at  $60^\circ\text{C}$  for 12 h and then treated in a muffle furnace at  $200^\circ\text{C}$  (heating rate of  $2^\circ\text{C min}^{-1}$ ) and kept for 2 h. Subsequently, the samples were calcined at  $700^\circ\text{C}$  for 2 h in a nitrogen atmosphere ( $5^\circ\text{C min}^{-1}$ ) and cooled down to less than  $30^\circ\text{C}$  to obtain the final catalysts, denoted as  $\text{Co}_1\text{Fe}_{1.5}/\text{C}$ . Meanwhile, other comparative samples  $\text{Co}_x\text{Fe}_y$  gained at different molar ratios (1:1, 1:2), 2.5 mmol pure Fe PAN spinning and 2.5 mmol pure Co PAN spinning were prepared respectively, denoted as  $\text{Co}_1\text{Fe}_1/\text{C}$ ,  $\text{Co}_1\text{Fe}_2/\text{C}$ ,  $\text{Fe}_{2.5}/\text{C}$ , and  $\text{Co}_{2.5}/\text{C}$ , respectively.

### 2.3. Characterizations

Field-emission Scanning Electron Microscopy (FESEM) was carried out on a S4800 equipment of Japan Hitachi. Transmission Electron Microscopy (TEM) was used by JEM-2010 EX equipment. The Fine X-ray Diffraction (XRD) pattern was performed using a SmartLab under a scan rate of  $2^\circ/\text{min}$ . Raman spectra were carried out on inVia of Renishaw Public Company. X-ray Photoelectron Spectroscopy (XPS) was revealed by EscaLab 250Xi equipment of Thermo Scientific Nexsa with  $\text{Al K}\alpha$  as the X-ray source. In-situ XPS spectra were measured with NO and operated at 50 W. Inductively coupled plasma mass spectrometry (ICP-

MS) was carried out by a Perkin Elmer Optima 2000DV. UV absorbance was recorded using a MAPADA PC-1800. The specific surface area and pore properties were calculated by Brunauer-Emmett-Teller (BET) and Barrett-Joyner-Halenda (BJH) techniques. Ammonia Temperature Programmed rise Desorption ( $\text{NH}_3$ -TPD) was performed on the chemisorption of PCA-1200.

### 2.4. Computational information

The Gibbs free energy and electronic structure were calculated using density-functional theory (DFT) with the Perdew-Burke-Ernzerhof (PBE) and the generalized gradient approximation (GGA) exchange-correlation functional by the Cambridge sequential total energy package (CASTEP) in Material Studio software. The energy cutoff for the plane-wave basis set was 490 eV. The convergence criteria for geometry optimization, electronic structure, and displacement were  $0.03 \text{ eV}/\text{\AA}$ ,  $1.0 \times 10^{-5} \text{ eV/atom}$ , and  $0.001 \text{ \AA}$ , respectively.

The appropriated lattice parameters of face-centered cubic Co, body-centered cubic Fe, and primitive cubic CoFe were separately  $a = b = c = 3.40 \text{ \AA}$ ,  $a = b = c = 2.75 \text{ \AA}$ , and  $a = b = c = 2.75 \text{ \AA}$ , close to corresponding experimental values of 3.54, 2.86 and  $2.86 \text{ \AA}$ . Based on the major diffraction peak in XRD patterns,  $3 \times 2$  periodic four CoFe atomic (110) layers ( $a = 8.2 \text{ \AA}$  and  $b = 7.7 \text{ \AA}$ ),  $3 \times 3$  periodic four Co atomic (111) layers ( $a = b = 7.2 \text{ \AA}$ ) and  $3 \times 2$  periodic four Fe atomic (110) layers ( $a = 8.2 \text{ \AA}$  and  $b = 7.7 \text{ \AA}$ ) were selected as the models of CoFe, Co and Fe particles respectively. The lower layers of Co(111), Fe(110), and CoFe(110) were fixed at the equivalent positions and other layers were

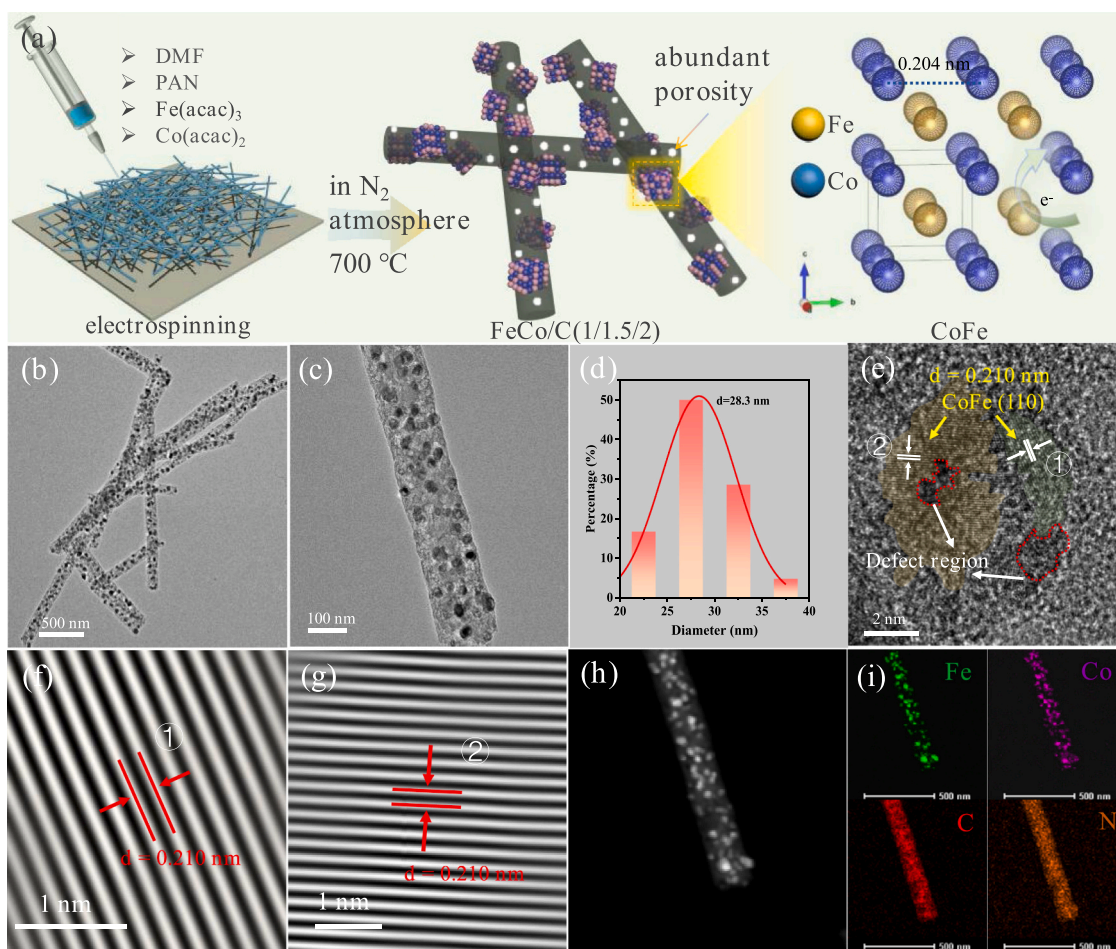


**Fig. 1.** (a) Synthetic illustration and details of CoFe/C catalyst, (b-c) TEM images of  $\text{Co}_1\text{Fe}_{1.5}/\text{C}$ , (d) statistics of FeCo nanoalloys size distribution over the porous carbon fibers. (e) HRTEM image of  $\text{Co}_1\text{Fe}_{1.5}/\text{C}$ , and (f-g) (110) lattice space of FeCo alloy in  $\text{Co}_1\text{Fe}_{1.5}/\text{C}$  extracted from Fast Fourier Transform. (h) HAADF-STEM image and (i) EDX elemental mapping images of Fe, Co, C, and N elements of  $\text{Co}_1\text{Fe}_{1.5}/\text{C}$ .



relaxed. A vacuum layer of 15 Å was along the z-direction was used to avoid interactions between the neighboring slabs.

### 3. Results and discussion

#### 3.1. Structure and characterization of materials

Fig. 1a shows the synthetic illustration of the CoFe/C catalyst based on the electrospinning technique, where PAN containing the organic metal precursor was electrospun to synthesize the polymer fiber followed by heat crosslinking and graphitized procedure. The FeCo precursors were transformed into alloying state with tuning FeCo fraction which in-situ confined in N-doping porous carbon fiber. Note that Fe precursors mainly play dual function roles working as catalytic centers and activators for constructing porous carbon. Fig. 1b,c, and S1a show the TEM images of  $\text{Co}_1\text{Fe}_{1.5}/\text{C}$  where CoFe alloy nanoparticles are uniformly distributed into carbon nanofibers (CNF) with an average diameter defined between 200 and 350 nm, such a tandem configuration is generally conducive to the electrons transfer during the electrochemical process[33]. The encapsulation of the nanoparticles by the carbon fibers helps to stabilize the nanoparticles and prevent aggregation of the particles. It also can stabilize the active sites, in turn, improving the catalytic performance. In addition, the tandem configuration of the CoFe nanoalloy over the porous carbon fibers makes them have enough exposure and possible electron transfer of each other, which is favorable for the surface adsorption and activation of  $\text{NO}_3^-$  and  $\text{NO}_2^-$ . The FeCo nanoalloys over the  $\text{Co}_1\text{Fe}_{1.5}/\text{C}$  are counted to afford an average particle size calculated to be ca. 27 nm (Fig. 1d). Such a refined size is generally enough active for the heterogeneous catalytic process but often requires protection of support to inhibit their aggregation and deactivation. The High-Resolution Transmission Electron Microscope

(HRTEM) image (Fig. 1e, f, g) shows that clear lattice fringes in the selected region are determined by fast Fourier transform (FFT) analysis. The crystal plane spacing measured is 0.210 nm, corresponding to the (110) crystal plane of CoFe alloys (JCPDS: 49–1568) (Figure1b). In contrast, a slight increase in the spacing between the (110) crystal faces of  $\text{Co}_1\text{Fe}_{1.5}/\text{C}$  can be identified, probably due to the over-substitution of the Fe atom in the FeCo alloy crystal structure. Note that the defective region can be found in the HRTEM image of FeCo nanoalloys, indicating the possibility of a more active catalytic interface existing over the nanoalloys. Meanwhile, to confirm the accurate composition state of CoFe alloy over carbon fibers, HAADF-STEM images and elemental mapping graphics (Fig. 1h, i) were collected, clearly validating the uniform distribution of the elements of C, N, Co, and Fe a good tandem structure of FeCo nanoalloys over  $\text{Co}_1\text{Fe}_{1.5}/\text{C}$  porous carbon fibers. Compared with monometallic  $\text{Fe}_{2.5}/\text{C}$  and  $\text{Co}_{2.5}/\text{C}$ , bimetallic CoFe alloying catalysts afford enlarged diameter of the carbon nanofibers, and carbon nanofibers become progressively coarser with the increase of the molar ratio of Co to Fe from 1:1–1:2 (Figure2, S3). In addition, the nitrogen adsorption and desorption curves of CoFe/C conform to the type IV behavior, indicating that the catalyst is dominated by mesoporous structure. The specific surface area of  $\text{Co}_1\text{Fe}_{1.5}/\text{C}$  was calculated to be  $606.47 \text{ m}^2 \text{ g}^{-1}$ , affording the well-developed disordered 3D network structure for the adsorption and transport of Nitrate with intermediates (Figure4, S5). Meanwhile, combined with the analysis of structural properties, it can be found that the combination of Fe and Co in the electrospinning process could trigger the bigger specific surface area of the catalyst, outperforming the monometallic counterparts. In particular, the rational Fe composition in alloyed catalysts contributes to the improved surface area, indicating the dominant activator role of Fe in determining the activation of activated carbon (Table S1).

Fig. 2a shows the refined X-ray diffraction (XRD) patterns of CoFe

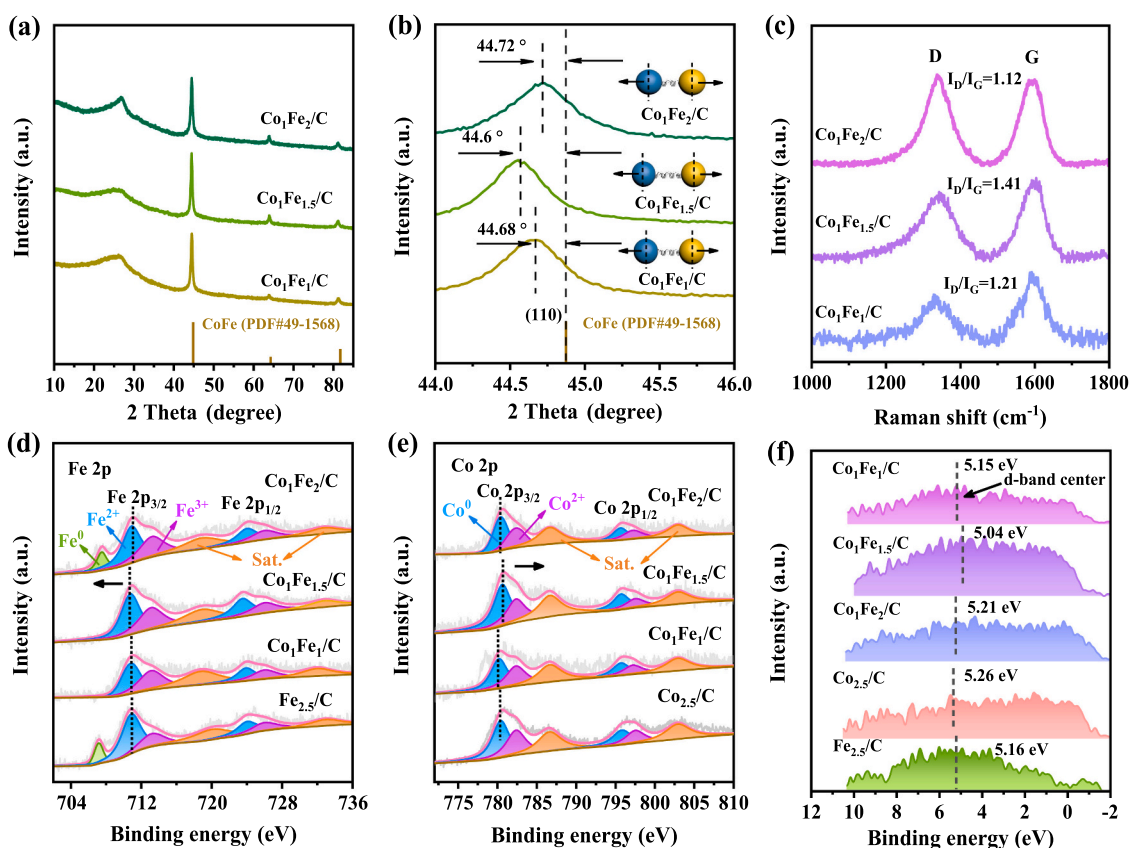


**Fig. 2.** (a-b) Fine XRD patterns of  $\text{Co}_1\text{Fe}_1/\text{C}$ ,  $\text{Co}_1\text{Fe}_{1.5}/\text{C}$ , and  $\text{Co}_1\text{Fe}_2/\text{C}$  samples. Raman spectra of (c)  $\text{Co}_1\text{Fe}_1/\text{C}$ ,  $\text{Co}_1\text{Fe}_{1.5}/\text{C}$ , and  $\text{Co}_1\text{Fe}_2/\text{C}$  samples. XPS spectra of (d) Fe 2p core level of  $\text{Fe}_{2.5}/\text{C}$  and CoFe/C series samples, (e) Co 2p core level of  $\text{Co}_{2.5}/\text{C}$  and CoFe/C series samples, and (f) XPS surface valence band spectra of the CoFe/C alloys,  $\text{Co}_{2.5}/\text{C}$  and  $\text{Fe}_{2.5}/\text{C}$ .

alloys (CoFe/C series). Co<sub>1</sub>Fe<sub>1.5</sub>/C is featured by several diffraction peaks located at 44.6°, 64.0°, and 81.3° corresponding to the (110), (200), and (211) planes of the CoFe alloy (JCPDS: 49-1568)[34]. In addition, the typical (002) peak at 20–30° belongs to the characteristic diffraction of graphitic carbon structure, derived from graphitized carbon nanofibres, indicative of the configuration of metal-carbon composites [16]. Notably, the position of the (110) diffraction peak of FeCo nanoalloys is shifted to the lower angle (44.9° → 44.6°) with respect to the standard FeCo alloying phase (JCPDS: 15-0806), suggesting that the alloying process with higher Fe composition substitution might make the lattice expansion of (110) crystal plane of FeCo nanoalloys, resulting in a longer Co-Fe bond length (Fig. 2b) [35], which is beneficial to the electron mobility and improved electrical conductivity of the catalysts. The refined XRD diffraction further demonstrates an angle shift near 0.3 rad that the range of offsets is within a convincing interval, which is rational to explain the lattice extension of the sample [36]. In addition, the monometallic comparison samples that Co<sub>2.5</sub>/C and Fe<sub>2.5</sub>/C were further analyzed (Figure 6a,b), the metallic phase Fe or Co can be identified for the respective samples, while the Fe<sub>2</sub>O<sub>3</sub> existed in Fe<sub>2.5</sub>/C possibly caused by the complex valence state of Fe itself leading to the partial oxidation of metallic Fe species. The Raman scattering of the CoFe/C series (Fig. 2c) shows that the peaks located near 1340 cm<sup>-1</sup> and 1600 cm<sup>-1</sup> correspond respectively to the D and G bands of the carbon skeleton, respectively. The relative intensity ratios of the peaks (I<sub>D</sub>/I<sub>G</sub>) can be used as a standard for evaluating the extent of carbon materials graphitization[37]. The calculated I<sub>D</sub>/I<sub>G</sub> values are in the order of Co<sub>1</sub>Fe<sub>2</sub>/C (1.12) < Co<sub>1</sub>Fe<sub>1</sub>/C (1.21) < Co<sub>1</sub>Fe<sub>1.5</sub>/C (1.41), and the high defects level of Co<sub>1</sub>Fe<sub>1.5</sub>/C is favorable for the stabilization of FeCo nanoalloys and surface adsorption of NO<sub>3</sub>. In addition, the calculated I<sub>D</sub>/I<sub>G</sub> values of Fe<sub>2.5</sub>/C and Co<sub>2.5</sub>/C are 1.07 and 1.25, respectively (Figure 7a,b). Such defects are possibly caused by doped N species in the carbon framework, evidenced by the N XPS spectra in Figure 9c, which can optimize the electronic structure of the nanoparticle surface by strong interaction and provide richer electrons to improve the affinity of the catalyst and the adsorption of Nitrate. The vibrational peaks of Co atoms are identified and located at ~ 504 cm<sup>-1</sup>, 385 cm<sup>-1</sup>, 275 cm<sup>-1</sup>, and 240 cm<sup>-1</sup>, corresponding to the A<sub>1g</sub>, 2 F<sub>2g</sub>, and E<sub>g</sub> modes[20,38], and the vibrational peaks of Fe atoms are located at ~ 677 cm<sup>-1</sup>, 511 cm<sup>-1</sup>, and 474 cm<sup>-1</sup>, corresponding to the A<sub>1g</sub>, T<sub>2g</sub>, and E<sub>g</sub> modes [39], respectively. The Raman peaks of Co and Fe in Co<sub>1</sub>Fe<sub>1.5</sub>/C both exhibit significant redshift compared to monometallic counterparts (Figure 8a,b), indicating that more defects can be created when CoFe alloying, possibly causing the improved adsorption of NO<sub>3</sub> and intermediates over defect sites in Co<sub>1</sub>Fe<sub>1.5</sub>/C[40]. Note that the weak vibrations of metal-O observed from Raman spectra may be associated with the existing metal-oxygen bond by the strong interaction between nanoalloy and oxygen species of edge position of carbon support.

X-ray photoelectron spectroscopy (XPS) was used to identify the chemical valency and electronic interactions of the prepared CoFe/C. The survey spectra of XPS (Figure 9a) show the main surface element composition of CoFe/C. The XPS spectra of C1s (Figure 9b) show three characteristic peaks at 288.6, 286.2, and 284.6 eV belonging to C=O, C=C, and C-C[41], respectively. The N 1s spectra in Figure 9c show the three types of N peaks including graphitic N (403.4 eV), pyrrolic N (400.4 eV), and pyridine N (398.3 eV)[42], with the highest graphitic N content (20.56 %) for Co<sub>1</sub>Fe<sub>1.5</sub>/C, and the increase in graphitic N is favorable for the improvement of the electrical conductivity. In addition, the pyrrole nitrogen content of Co<sub>1</sub>Fe<sub>1.5</sub>/C was calculated to be the highest, reaching 59.88 % (Figure 9c), which favors the affinity and adsorption of NO<sub>3</sub>. [43] The XPS of Fe<sub>2.5</sub>/C and Co<sub>2.5</sub>/C were also studied as control samples (Fig. 2d, e, S10, S11). By comparing the N XPS spectra of Fe<sub>2.5</sub>/C and Co<sub>2.5</sub>/C, it is found that Fe<sub>2.5</sub>/C has a higher pyrrolic N site for better Nitrate adsorption. Fe<sub>2.5</sub>/C exhibits three sets of Fe 2p characteristic peaks, with binding energies of 713.11 eV, 710.85 eV, and 707.15 eV corresponding to Fe<sup>3+</sup>, Fe<sup>2+</sup> and Fe<sup>0</sup>, [44] respectively (Fig. 2d). With the alloying CoFe species in the samples, the binding

energies of Fe(II) 2p<sub>3/2</sub> and Fe(II) 2p<sub>1/2</sub> in Co<sub>1</sub>Fe<sub>1.5</sub>/C shifts to 723.5 eV and 710.75 eV, respectively (Fig. 2d), suggesting a strong electronic coupling between Fe and Co in the alloys. The lower Fe 2p binding energy spectra of Co<sub>1</sub>Fe<sub>1.5</sub>/C suggests that Fe, through alloying with Co, thus gains more electrons. Similarly, the XPS of Co<sub>1</sub>Fe<sub>1</sub>/C exhibits a negative shift of Fe 2p<sub>3/2</sub> and Fe 2p<sub>1/2</sub> to lower binding energy. The Co 2p XPS spectrum is shown in Fig. 2e, Co<sub>2.5</sub>/C exhibits two sets of Co 2p characteristic peaks with binding energies of 782.3 eV and 780.3 eV belonging to the Co<sup>2+</sup> and Co<sup>0</sup> [45], respectively (Fig. 2e). In Co<sub>1</sub>Fe<sub>1.5</sub>/C and Co<sub>1</sub>Fe<sub>1</sub>/C, the binding energy values corresponding to Co<sup>0</sup> show positive shifts, 0.3 eV for Co<sub>1</sub>Fe<sub>1.5</sub>/C and 0.1 eV for Co<sub>1</sub>Fe<sub>1</sub>/C (Fig. 2e, Table S2), suggesting that the electronic interactions between Co and Fe atoms are stronger and the electron-deficient Co centers are favorable for the adsorption of NO<sub>3</sub> and intermediate in the NO<sub>3</sub>RR process (Table S2). It is worth mentioning that the introduction of excess Fe in Co<sub>1</sub>Fe<sub>2</sub>/C causes the opposite tendency to Co<sub>1</sub>Fe<sub>1.5</sub>/C and Co<sub>1</sub>Fe<sub>1</sub>/C, Co<sub>1</sub>Fe<sub>2</sub>/C exhibits a positive displacement of Fe XPS versus a negative displacement of Co XPS, which leads to the difficulty in adsorption of NO<sub>3</sub> over Co active center, thus reducing NO<sub>3</sub>RR activity. Interestingly, a higher proportion of Fe<sup>2+</sup> in Co<sub>1</sub>Fe<sub>1.5</sub>/C was evidenced by XPS of the Fe region. We suggest that the asymmetric distribution of the 3d orbital electrons of Fe<sup>2+</sup> is due to the emergence of the surface oxidation state leads to the Jahn-Teller effect to eliminate this degenerate orbital, possibly causing the expansion of the crystal lattice and change in bond length. To prove the conclusion drawn from the XPS spectra, we further calculated and predicted the shift of the location of the d-band center by XPS valence band spectra. Note that the d-band center of the Co catalyst increases from 5.26 eV to 5.04 eV when alloying with Fe (Fig. 2 f), showing that the introduction of Fe makes the middle location of the valence band integral move to the Fermi energy level, leading to easier adsorption and activation of NO<sub>3</sub>. [46]

### 3.2. NO<sub>3</sub>RR performance and analysis

The NO<sub>3</sub>RR activity of all the samples was measured by a standard three-electrode system in a neutral electrolyte [0.05 M NO<sub>3</sub> (KNO<sub>3</sub>) and 1 M K<sub>2</sub>SO<sub>4</sub>] in an H-type electrolyzer at 400 rpm for 1 h. All overpotentials were corrected by RHE and all experiments were treated after three repetitions. With the proceeding of electrocatalytic NO<sub>3</sub>RR for 1 h, the used electrolyte was diluted to the detection line, and the NO<sub>3</sub>-N, NH<sub>3</sub>-N, and NO<sub>2</sub>-N concentrations were quantified by colorimetric assay, and the standard curves are detailed in the SI Appendix (Figure S12,13, 14). We first used linear scanning voltammetry (LSV) in K<sub>2</sub>SO<sub>4</sub> electrolytes with or without KNO<sub>3</sub> to identify the catalytic activity of Nitrate reduction over Co<sub>1</sub>Fe<sub>1.5</sub>/C (Fig. 3a). The current density of the KNO<sub>3</sub>-containing electrolyte was increased at the identical potential, indicating that Co<sub>1</sub>Fe<sub>1.5</sub>/C could effectively reduce NO<sub>3</sub> ions by the accelerated electron transfer in the electrocatalytic process[47], outperforming the other counterparts including Co<sub>1</sub>Fe<sub>1</sub>/C, Co<sub>1</sub>Fe<sub>2</sub>/C, Fe<sub>2.5</sub>/C, and Co<sub>2.5</sub>/C (Figure 15). Then, the tendency of current density evolution in LSV measurements of Co<sub>1</sub>Fe<sub>1.5</sub>/C was obtained at a given electrode potential range of -0.8 V to -1.2 V vs. RHE. The negligible change in current i-t curves at different electrode potentials for 1 h demonstrates good catalytic stability of Co<sub>1</sub>Fe<sub>1.5</sub>/C during the NO<sub>3</sub>RR process even in varying NO<sub>3</sub> concentrations (Figure 16). The NH<sub>3</sub> yield and Faraday efficiency of Co<sub>1</sub>Fe<sub>1.5</sub>/C gradually increase with increasing voltage (Fig. 3b), delivering the highest NH<sub>3</sub> yield (48.2 ± 1.2 mg h<sup>-1</sup> mg<sub>cat</sub><sup>-1</sup>) as well as the highest Faraday efficiency (90.8 ± 1.5 %) when at -1.1 V vs. RHE. When the operated voltage is less than -1.1 V vs. RHE, NO<sub>2</sub> was probably the major product, however, NH<sub>3</sub> yield and FE started to decrease significantly with increased operated voltage, possibly due to the HER competition at the high potentials. In addition, the effect of the reaction environment on the performance of NO<sub>3</sub>RR at different NO<sub>3</sub> reaction concentrations (0.02, 0.05, and 0.1 M) as well as at different stirring speeds (200, 400, and 600 rpm) was explored to determine the optimal reaction conditions (Fig. 3c,d, S16, S17). Comparison in NO<sub>3</sub>RR

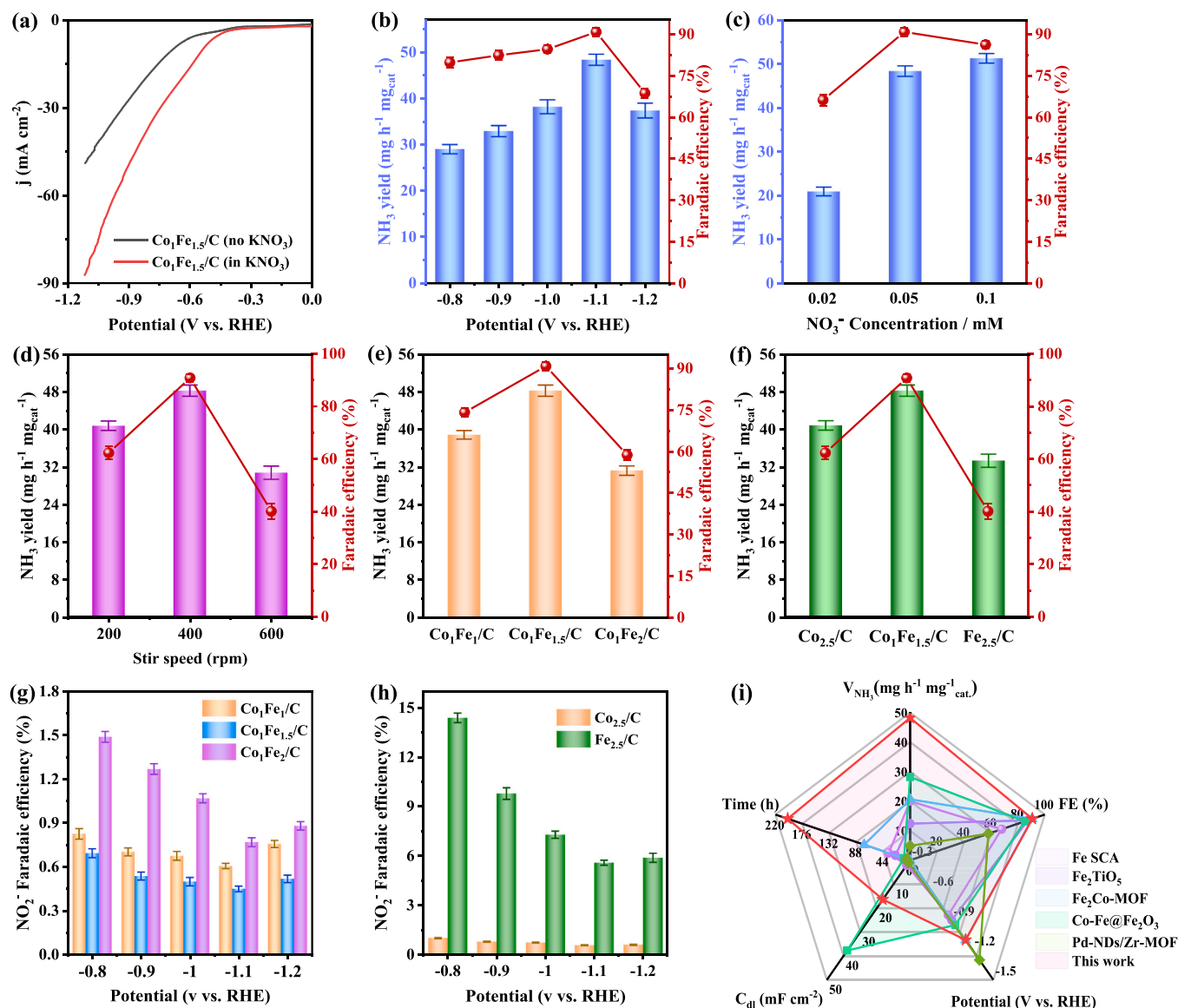


**Fig. 3.** Electrochemical performance of catalysts for 1 h of NO<sub>3</sub>RR electrolysis. (a) LSV curves of Co<sub>1</sub>Fe<sub>1.5</sub>/C in 1 M K<sub>2</sub>SO<sub>4</sub> solution with and without NO<sub>3</sub><sup>-</sup> (0.05 M). (b) Potential-dependent FE and NH<sub>3</sub> yield rate for Co<sub>1</sub>Fe<sub>1.5</sub>/C. (c) Comparison of FE and NH<sub>3</sub> yield rate for the Co<sub>1</sub>Fe<sub>1.5</sub>/C catalyst at different NO<sub>3</sub><sup>-</sup> concentrations. (d) FE and NH<sub>3</sub> yield rate of the Co<sub>1</sub>Fe<sub>1.5</sub>/C catalyst with different stirring speeds. (e) and (f) Comparison of FE and NH<sub>3</sub> yield of different materials. Faraday efficiency of NO<sub>2</sub><sup>-</sup> on different samples: (g) Co<sub>1</sub>Fe<sub>1</sub>/C, Co<sub>1</sub>Fe<sub>1.5</sub>/C and Co<sub>1</sub>Fe<sub>2</sub>/C samples, (h) Co<sub>2.5</sub>/C and Fe<sub>2.5</sub>/C samples. (i) Comparison in FE and NH<sub>3</sub> yield of Co<sub>1</sub>Fe<sub>1.5</sub>/C with the reported NO<sub>3</sub>RR electrocatalysts (detailed data in [Supporting Information](#)).

performance of Co<sub>1</sub>Fe<sub>1</sub>/C, Co<sub>1</sub>Fe<sub>1.5</sub>/C, and Co<sub>1</sub>Fe<sub>2</sub>/C (Fig. 3e, S18) shows the obvious advantages of Co<sub>1</sub>Fe<sub>1.5</sub>/C in the NH<sub>3</sub> yield and FE compared to those of Co<sub>1</sub>Fe<sub>1</sub>/C ( $38.8 \pm 1.8 \text{ mg h}^{-1} \text{ mg}_{\text{cat}}^{-1}$  and  $74.1 \pm 1.5 \%$ ) and Co<sub>1</sub>Fe<sub>2</sub>/C ( $30.4 \pm 2.6 \text{ mg h}^{-1} \text{ mg}_{\text{cat}}^{-1}$  and  $58.7 \pm 1.8 \%$ ). In addition, the synergetic advantage of alloyed bimetals of Co<sub>1</sub>Fe<sub>1.5</sub>/C in the NO<sub>3</sub>RR process can be further demonstrated when compared with Co<sub>2.5</sub>/C and Fe<sub>2.5</sub>/C (Fig. 3f, S19). Meanwhile, the possible by-products examination of NO<sub>2</sub> (Fig. 3g, h), indicates the NO<sub>2</sub> minimized at  $-1.1 \text{ V}$  vs. RHE, demonstrating the excellent selectivity of Co<sub>1</sub>Fe<sub>1.5</sub>/C for NH<sub>3</sub>. Interestingly, the activity of NO<sub>3</sub>RR shows a volcano-type evolution trend with increasing Fe molar ratio in CoFe/C within a certain range. Combined with the above characterization analysis, it suggests that the alloying of Fe with Co can modulate the electronic structure of Co and improve the selectivity of intermediate adsorption, which further enhances the NO<sub>3</sub>RR activity [45]. Notably, the NH<sub>3</sub> yield and FE achieved by Co<sub>1</sub>Fe<sub>1.5</sub>/C are compared with most reported state-to-the-art NO<sub>3</sub>RR catalysts employed at high reaction potential ( $>0.9 \text{ V}$ ) (Fig. 3i, Table S5). The results demonstrated that the catalysts still possessed

significant FE with long-lasting long-time tests under high overpotential conditions, indicating that the catalysts have a clear advantage over other catalysts in terms of selectivity and stability. This excellent NH<sub>3</sub> yield and FE at high reaction potential further highlight the superiority and potential of the Co<sub>1</sub>Fe<sub>1.5</sub>/C in the NO<sub>3</sub>RR application. In addition, Co<sub>1</sub>Fe<sub>1.5</sub>/C can still showcase significant NO<sub>3</sub>RR performance advantages over traditional Co- or Fe-based bimetallic or alloy catalysts and even outperform some noble metal-based catalysts. Despite being compared to some state-to-art catalysts, a significant advantage in terms of the long-term stability (200 h) for Co<sub>1</sub>Fe<sub>1.5</sub>/C should still be highlighted.

### 3.3. Identification of NO<sub>3</sub>RR kinetics

To clearly reveal the content of each intermediate component in the electrolyte of CoFe/C and the comparison samples during the NO<sub>3</sub>RR process, the dynamic analysis based on K<sub>2</sub>SO<sub>4</sub> containing 100 ppm KNO<sub>3</sub> was performed, and Fig. 4a shows the dynamic variation of NO<sub>3</sub>-

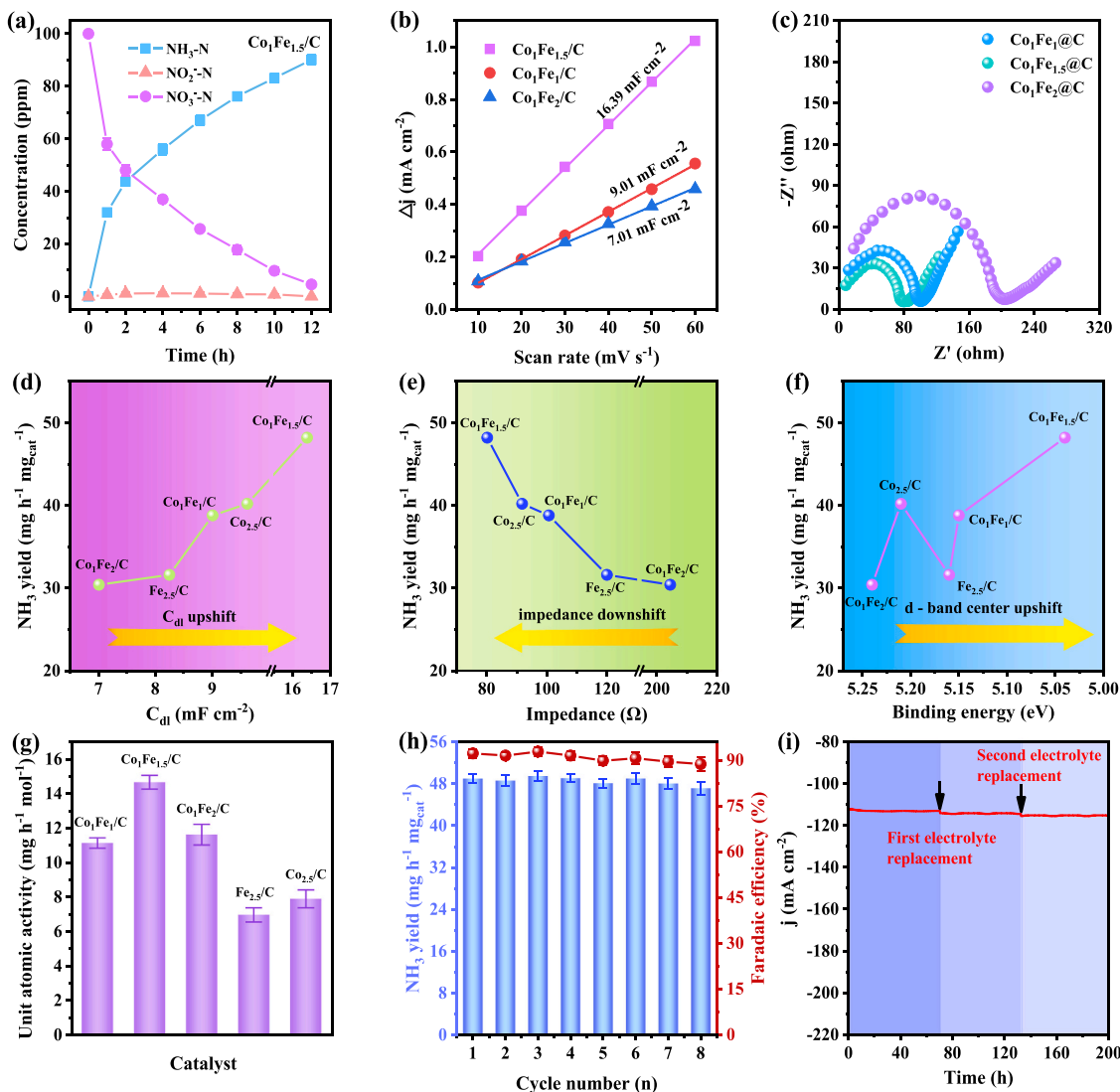


**Fig. 4.** (a) Real-time dynamic analysis of  $\text{Co}_1\text{Fe}_{1.5}/\text{C}$  (in 100 ppm  $\text{NO}_3^-$ ), (b) Determination of electrochemical double-layer capacitance ( $C_{dl}$ ), and (c) Nyquist plots for  $\text{Co}_1\text{Fe}_1/\text{C}$ ,  $\text{Co}_1\text{Fe}_{1.5}/\text{C}$  and  $\text{Co}_1\text{Fe}_2/\text{C}$  samples. Constitutive relationship diagram of electrochemical properties, (d) Relationships between  $\text{NH}_3$  yield versus electrochemical specific surface area (ECSA), (e) Relationships between  $\text{NH}_3$  yield versus electrochemical impedance (ECR), and (f) Relationships between  $\text{NH}_3$  yield versus the d-band center. (g) Comparison of atom normalized activity of different electrocatalysts. (h) Consecutive recycling test at  $-1.1$  V for  $\text{Co}_1\text{Fe}_{1.5}/\text{C}$ , (i) long-term  $\text{NO}_3\text{RR}$  electrolysis (the black arrow represents new electrolyte replacement).

$\text{N}$ ,  $\text{NO}_2\text{-N}$ , and  $\text{NH}_3\text{-N}$  concentrations with the prolonged time. At a constant voltage of  $-1.1$  V vs. RHE, the  $\text{NO}_3^-$  concentration in the  $\text{Co}_1\text{Fe}_{1.5}/\text{C}$  electrocatalyst-containing electrolyte decreases from 100 ppm to 4.6 ppm in 12 h, with a  $\text{NO}_3^-$  conversion of  $\sim 96.4 \pm 0.8$  %. The  $\text{NH}_3$  concentration increases steadily, reaching 91 ppm after 12 h, resulting from the conversion of  $\text{NO}_3^-$  to  $\text{NH}_3$ . Meanwhile, the intermediate  $\text{NO}_2^-$  concentration during the reaction is negligible, indicating that the  $\text{Co}_1\text{Fe}_{1.5}/\text{C}$  electrocatalyst was highly selective to Ammonia synthesis, up to  $\sim 94.4 \pm 1.2$  %. The catalytic performances of  $\text{Co}_1\text{Fe}_1/\text{C}$ ,  $\text{Co}_1\text{Fe}_2/\text{C}$ ,  $\text{Fe}_{2.5}/\text{C}$ , and  $\text{Co}_{2.5}/\text{C}$  are further compared (Figure 20, S21). The  $\text{NO}_3^-$  conversion and  $\text{NH}_3$  yield of  $\text{Co}_1\text{Fe}_{1.5}/\text{C}$  are significantly higher than those of the other counterparts, and the lowest electrocatalytic performance is observed for  $\text{Co}_1\text{Fe}_2/\text{C}$ , which was in agreement with the previous electronic structure analysis of CoFe/C series catalysts. In addition, the comparison shows that Co has superior selectivity for  $\text{NH}_3$  compared to Fe, in line with the expectation of the catalyst design.

The electrochemical surface areas (ECAs) associated related to the catalytic activity were calculated from the double-layer capacitance ( $C_{dl}$ ) obtained by cyclic voltammetry (CV) at different scan rates, as shown in the CV measurements ( $-0.2$  V to  $-0.4$  V vs. RHE) in Figure 22,

S23. The CV curve was obtained in the scan rate range of  $10 \sim 60$   $\text{mV s}^{-1}$ , as shown in Fig. 4b, the ECSA of  $\text{Co}_1\text{Fe}_{1.5}/\text{C}$  ( $16.39$   $\text{mF cm}^{-2}$ ) is obviously higher than that of  $\text{Co}_1\text{Fe}_1/\text{C}$  ( $9.01$   $\text{mF cm}^{-2}$ ),  $\text{Co}_1\text{Fe}_2/\text{C}$  ( $7.01$   $\text{mF cm}^{-2}$ ),  $\text{Co}_{2.5}/\text{C}$  ( $9.62$   $\text{mF cm}^{-2}$ ) and  $\text{Fe}_{2.5}/\text{C}$  ( $8.25$   $\text{mF cm}^{-2}$ ) (Figure 23c), indicating that tunable CoFe alloying with changed molar ratio improves the ECSA and therefore positively affects  $\text{NO}_3\text{RR}$  catalytic activity with higher electron transfer capacity. Demonstrating catalytic kinetics can be effectively evidenced by Electrochemical Impedance Spectroscopy (EIS) [48]. Nyquist plots of  $\text{Co}_1\text{Fe}_{1.5}/\text{C}$ ,  $\text{Co}_1\text{Fe}_1/\text{C}$ , and  $\text{Co}_1\text{Fe}_2/\text{C}$  were obtained using Electrochemical Impedance Spectroscopy (Fig. 4c). The smaller radius of the Nyquist plots indicates the faster the interfacial electron transfer. In addition, the slope of the polarization is related to the proof against corrosion of the material, the larger the slope of the polarization corresponds to the stronger corrosion resistance of the material. The Nyquist plots show that the arc radius of  $\text{Co}_1\text{Fe}_{1.5}/\text{C}$  is the smallest ( $80.2$   $\Omega$ ) among the prepared catalysts, which is much less than that of  $\text{Co}_1\text{Fe}_1/\text{C}$  ( $100.7$   $\Omega$ ) and  $\text{Co}_1\text{Fe}_2/\text{C}$  ( $204.5$   $\Omega$ ), indicating a low resistance to charge transfer. This result further suggests that the alloying of CoFe with lattice expansion can modulate the electronic structure of Co thereby



improving the charge transfer at the cathode, favorable for NO<sub>3</sub>RR, also agreeing with the previous XRD analysis. In addition, the Nyquist plots of Fe<sub>2.5</sub>/C and Co<sub>2.5</sub>/C are shown in Figure 24, further indicating the advantage of the Co<sub>1</sub>Fe<sub>1.5</sub>/C. In addition, Co<sub>1</sub>Fe<sub>1.5</sub>/C is demonstrated to afford the largest polarization slope, indicating that the tuning CoFe alloying is also conducive to improving the corrosion resistance of the catalysts, which has excellent potential for practical applications. Based on the above results, we summarized the constitutive relationship plots between electrocatalytic activity and C<sub>dl</sub> and impedance, (Fig. 4d,e) in which we can clearly identify the effects of C<sub>dl</sub> and impedance on the electrocatalytic performance, with the electrochemical specific surface area proportional to the electrocatalytic performance and the impedance on the contrary. In addition, we also compared the electrochemical performance with the position of the calculated d-band center of the catalyst obtained by XPS surface valence spectra (Fig. 4f), the electrocatalytic performance basically shows a gradual enhancement as the d-band center gets closer to the Fermi energy level. This indicates that the decrease of the d-band center of active species can effectively reduce the energy barrier of electron transfer in the reaction process, optimize the electronic transfer efficiency, and thus improve the electrocatalytic performance. Furthermore, the overpotential of the catalyst can be tailored by combining the FeCo alloying determined by engineering. By comparing the overpotentials of the individual catalysts at different current densities, it is clear that CoFe all have the lowest overpotentials. It is demonstrated that FeCo alloying optimizes the electronic structure of Co and lowers the reaction energy barrier, thus reducing the energy consumption during the reaction, which is conducive to the improvement of electrocatalytic performance (Figure 25). These above factors make the Co<sub>1</sub>Fe<sub>1.5</sub>/C become optimal catalytic for achieving NO<sub>3</sub>RR performance.

To explore the source of activity induced by catalysts with diverse metal ratios, we measured the metal contents of the CoFe/C catalysts at different ratios based on Inductively coupled plasma (ICP) measurements (Table S3). It is suggested that the Co/Fe ratios of the different catalysts are basically in accordance with the molar ratios of the initial amount of precursor salts added. The total metal content of Co<sub>1</sub>Fe<sub>1.5</sub>/C was measured at 37.83 wt % in the composite. To determine the normalized atomic activity in the NO<sub>3</sub>RR, the NH<sub>3</sub> yields of per mol metal active sites in different electrocatalysts were further calculated. The normalized NH<sub>3</sub> yield of Co<sub>1</sub>Fe<sub>1.5</sub>/C catalyst was calculated as high as 14.7 mg h<sup>-1</sup> mol<sub>CoFe</sub><sup>-1</sup>, which was obviously higher than that of Co<sub>1</sub>Fe<sub>1</sub>/C (11.1 mg h<sup>-1</sup> mol<sub>CoFe</sub><sup>-1</sup>), Co<sub>1</sub>Fe<sub>2</sub>/C (11.6 mg h<sup>-1</sup> mol<sub>CoFe</sub><sup>-1</sup>), Fe<sub>2.5</sub>/C (6.9 mg h<sup>-1</sup> mol<sub>Fe</sub><sup>-1</sup>) and Co<sub>2.5</sub>/C (7.9 mg h<sup>-1</sup> mol<sub>Co</sub><sup>-1</sup>) (Fig. 4g). This result demonstrates that the origin in enhancement of activity is mainly from the electronic structural optimization of alloyed CoFe and possible improved electrical conductivity of the Co<sub>1</sub>Fe<sub>1.5</sub>/C catalysts accelerating the electron transfer process, thereby facilitating the electrocatalytic NO<sub>3</sub>RR reaction rapidly. During eight NO<sub>3</sub>RR reaction cycles of Co<sub>1</sub>Fe<sub>1.5</sub>/C, both NH<sub>3</sub> yield and FE still show good consistency (Fig. 4h, S26), which further indicates the excellent electrocatalytic stability and reproducibility of Co<sub>1</sub>Fe<sub>1.5</sub>/C electrocatalyst. Since the possible negative influence of Nitrate ion concentration reduction on the reaction dynamics and change in current density in the actual reaction, we regenerated three consecutive current i-t curves test graphs by changing the electrolyte twice during the long-time stability test [49]. The i-t curve measurement indicates that 200 h electrolyzation for NO<sub>3</sub>RR can be attained over Co<sub>1</sub>Fe<sub>1.5</sub>/C under optimal conditions (Fig. 4i) without obvious downward decay of current density, validating the long-term stability of Co<sub>1</sub>Fe<sub>1.5</sub>/C in NO<sub>3</sub>RR. Meanwhile, the NH<sub>3</sub> yield and Faraday efficiency of the spent catalyst after a 200 h reaction are again compared with that of the brand-new Co<sub>1</sub>Fe<sub>1.5</sub>/C catalyst, showing a slight activity decrement (Figure 27), further indicating the excellent stability of Co<sub>1</sub>Fe<sub>1.5</sub>/C. The structure and valence of Co<sub>1</sub>Fe<sub>1.5</sub>/C before and after electrocatalysis were further checked using SEM, XRD, and XPS, wherein, Figure 28 shows that the spent Co<sub>1</sub>Fe<sub>1.5</sub>/C electrocatalyst still maintains the morphology of

nanofibers. Meanwhile, XRD characterization of Co<sub>1</sub>Fe<sub>1.5</sub>/C after the NO<sub>3</sub>RR reaction demonstrates the great reservation of alloyed CoFe in the catalyst despite undergoing the reaction (Figure 29). In addition, the XPS spectra reveal that the C 1s and N1s spectra before and after the NO<sub>3</sub>RR test were basically unchanged (Figure S30a, b). Note that the Fe<sup>2+</sup> peak is negatively shifted and the area ratio of the Fe<sup>3+</sup> peak is significantly increased after the reaction, while on the contrary, the Co<sup>0</sup> peak was positively shifted (Figure. S30c, d). Through this series of changes, we are inclined to speculate that the strong interaction between the Co and Fe atoms after the alloying of CoFe leads to part of the electron transfer from Fe to Co, thereby resulting in the increase of the positive charge at the Co center. This change is believed to favor the promotion of NO<sub>3</sub>RR, which coincides with the conclusions obtained earlier. Taken together, we suggest that the excellent NO<sub>3</sub>RR activity of Co<sub>1</sub>Fe<sub>1.5</sub>/C is related to its unique CoFe alloying configuration with a reduced d-band center confined into the disordered 3D N-doping carbon network structure, thereby improving the efficiency and selectivity of NO<sub>3</sub>RR. In particular, the alloying of Fe optimizes the electronic structure of Co, thereby enhancing the electrical conductivity of Co<sub>1</sub>Fe<sub>1.5</sub>/C, accelerating the ion diffusion rate, and improving its stability.

To exclude other potential sources of nitrogen affecting the NO<sub>3</sub>RR results, such as catalyst self-decomposition, electrolyte, or environmental conditions, the controlled tests were performed under open circuit voltage conditions, in K<sub>2</sub>SO<sub>4</sub> solution without Nitrate, and under normal reaction conditions, respectively. It can be observed that the Ammonia yield is negligible in the open circuit voltage and the Nitrate-free K<sub>2</sub>SO<sub>4</sub> solution, and was only observed in the conditions with the electrolyte in the presence of Nitrate (Figure 31). In addition, the source of nitrogen was intuitively identified using the <sup>15</sup>N isotope labeling method by analyzing the electrolyte after a 5 h reaction. When K<sup>15</sup>NO<sub>3</sub> was used as the electrolyte, a bimodal state corresponding to <sup>15</sup>NH<sub>4</sub><sup>+</sup> at δ = 6.78 and 6.96 ppm appeared. In contrast, a triplet state corresponding to <sup>14</sup>NH<sub>4</sub><sup>+</sup> was observed at δ = 6.74, 6.88, and 7.02 ppm (Figure 32) when using K<sup>14</sup>NO<sub>3</sub>.

The interaction ability of Ammonia over the surface of the prepared electrocatalysts was measured by Ammonia-programmed temperature desorption (NH<sub>3</sub>-TPD) (Fig. 5a, b). Compared with other samples, NH<sub>3</sub> affords the lowest desorption temperature on the surface of Co<sub>1</sub>Fe<sub>1.5</sub>/C, possibly making the produced NH<sub>3</sub> desorb more rapidly to expose the catalytic center for the next reaction cycle, which promotes the dynamic behavior. Meanwhile, to determine the surface adsorption behavior of different catalysts, the physical adsorption course curves of quantitative catalysts (5 mg) for NO<sub>3</sub> at ambient conditions were collected (Figure 33), indicating that Co<sub>1</sub>Fe<sub>1.5</sub>/C can afford the highest NO<sub>3</sub> affinity and adsorption capacity compared to other counterparts, which could trigger the accelerated dynamic process during the NO<sub>3</sub>RR. In addition, the adsorption of Fe<sub>2.5</sub>/C for NO<sub>3</sub> is greater than that of Co<sub>2.5</sub>/C at the same time, which indicates that Fe has better adsorption effect for NO<sub>3</sub>, consistent with the previous XPS results. Combined with these characterizations above, it can be inclined to conclude that the successful alloying of CoFe can significantly enhance the electronic coupling between Co and Fe and improve the electronic structure of the Co center, which not only promotes the adsorption of intermediates during the NO<sub>3</sub>RR process, but also facilitates the desorption of the product NH<sub>3</sub>, and this benign cycle of adsorption-desorption might be beneficial to improve the performance of Co<sub>1</sub>Fe<sub>1.5</sub>/C for NO<sub>3</sub>RR.

We also investigated the charge transfer process of Co<sub>1</sub>Fe<sub>1.5</sub>/C electrocatalyst in NO atmosphere using in situ XPS. Figure. S34a, b show the comparative XPS spectra of C1s and N1s in Co<sub>1</sub>Fe<sub>1.5</sub>/C in the presence as well as in the absence of NO, and it can be seen that due to the adsorption of NO on the surface, there is an extremely high N=O bonding peak at 405.8 eV, which leads to a substantial decrease in the content of other N species. In addition, the Fe 2p and Co 2p spectra of Co<sub>1</sub>Fe<sub>1.5</sub>/C (Fig. 5c, d) indicate the shift of binding energy of Co<sup>0</sup> in the presence of NO atmosphere excluding Fe, validating the interaction of Co with NO to gain electrons, correspondingly, the binding energy is



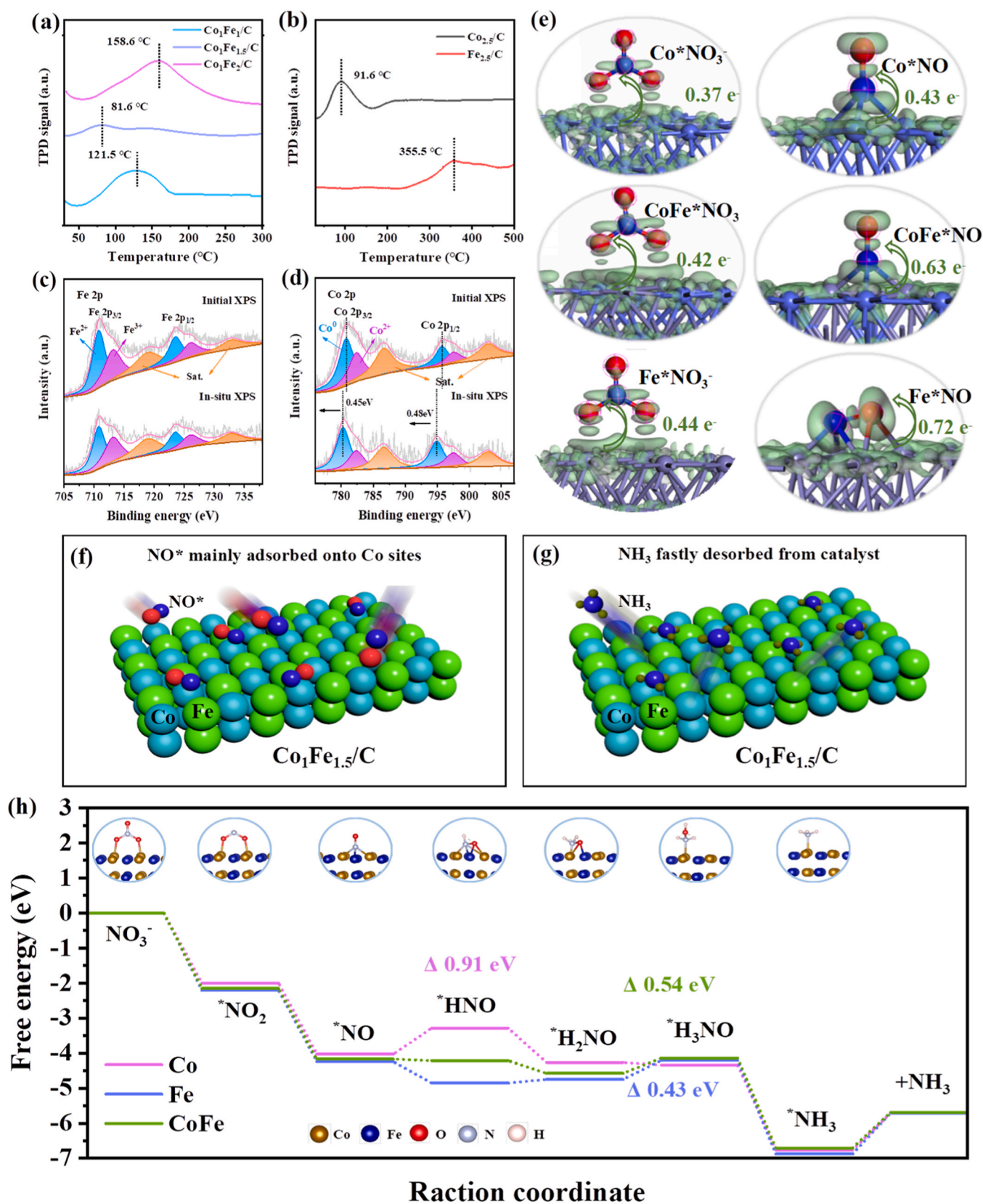


**Fig. 5.**  $\text{NH}_3$ -TPD profiles of different samples: (a)  $\text{Co}_1\text{Fe}_{1.5}/\text{C}$ ,  $\text{Co}_1\text{Fe}_{1.5}/\text{C}$ ,  $\text{Co}_1\text{Fe}_{1.5}/\text{C}$  samples, (b)  $\text{Co}_{2.5}/\text{C}$  and  $\text{Fe}_{2.5}/\text{C}$  samples. Comparison of XPS with in-situ XPS spectra of  $\text{Co}_1\text{Fe}_{1.5}/\text{C}$  electrocatalyst in the presence of near-atmospheric pressure NO; (c) Fe 2p and (d) Co 2p core levels. (e) Charge density differences and charge transfer of  $\text{NO}_3^-$  and  $\text{NO}^*$  adsorbed onto Co, Fe, and CoFe nanoalloy, respectively. Blue color indicates nitrogen atoms and red color indicates oxygen atoms. (f) Schematic illustration for NO preferably adsorbed onto Co sites of  $\text{Co}_1\text{Fe}_{1.5}/\text{C}$ , (g)  $\text{NH}_3$  fastly desorbed from the alloy surface of catalyst  $\text{Co}_1\text{Fe}_{1.5}/\text{C}$ . (h) Reaction-free energies for different intermediates on a Co, Fe, and CoFe alloy surface.

shifted to a lower energy level because the increasing electron cloud density, in turn, the adsorbed NO loses electrons, which is vulnerable to N-O bond breaking. In conjunction with the reported study that hydrogen-prone metals such as Co are favorable for subsequent hydrogenation steps[45], we can assume that Co acting as the main active site in the NO<sub>3</sub> reduction process is beneficial for the N-O bond breaking and hydrogenation process during the reaction (Fig. 5f, g). In addition, the above in-situ XPS experiment also demonstrates the dominant adsorption of NO over Co sites rather than Fe.

The Density Functional Theory (DFT) calculation study was employed to further understand the reaction mechanism of NO<sub>3</sub>RR on

different catalytic centers. Fig. 5e shows differential charge distribution results, in which the charge transfer behavior of \*NO<sub>3</sub> species and \*NO species over Co, Fe, and CoFe alloy models are measured to be 0.37, 0.42, 0.44 and 0.43, 0.72, 0.63 e<sup>-</sup>, respectively. It shows that the electron cloud density between NO<sub>3</sub> adsorbed onto CoFe is larger than that for Co or Fe, indicating the stronger electronic interaction between NO<sub>3</sub> and CoFe. In addition, this result suggests that Fe has a stronger trapping capacity for NO<sub>3</sub> compared to Co metal. Therefore, Fe alloying Co improved the \*NO<sub>3</sub> substance adsorbed on the surface of CoFe to a certain extent, which in turn reduces the impact of hydrogen precipitation competition. This promotes the production of the key active

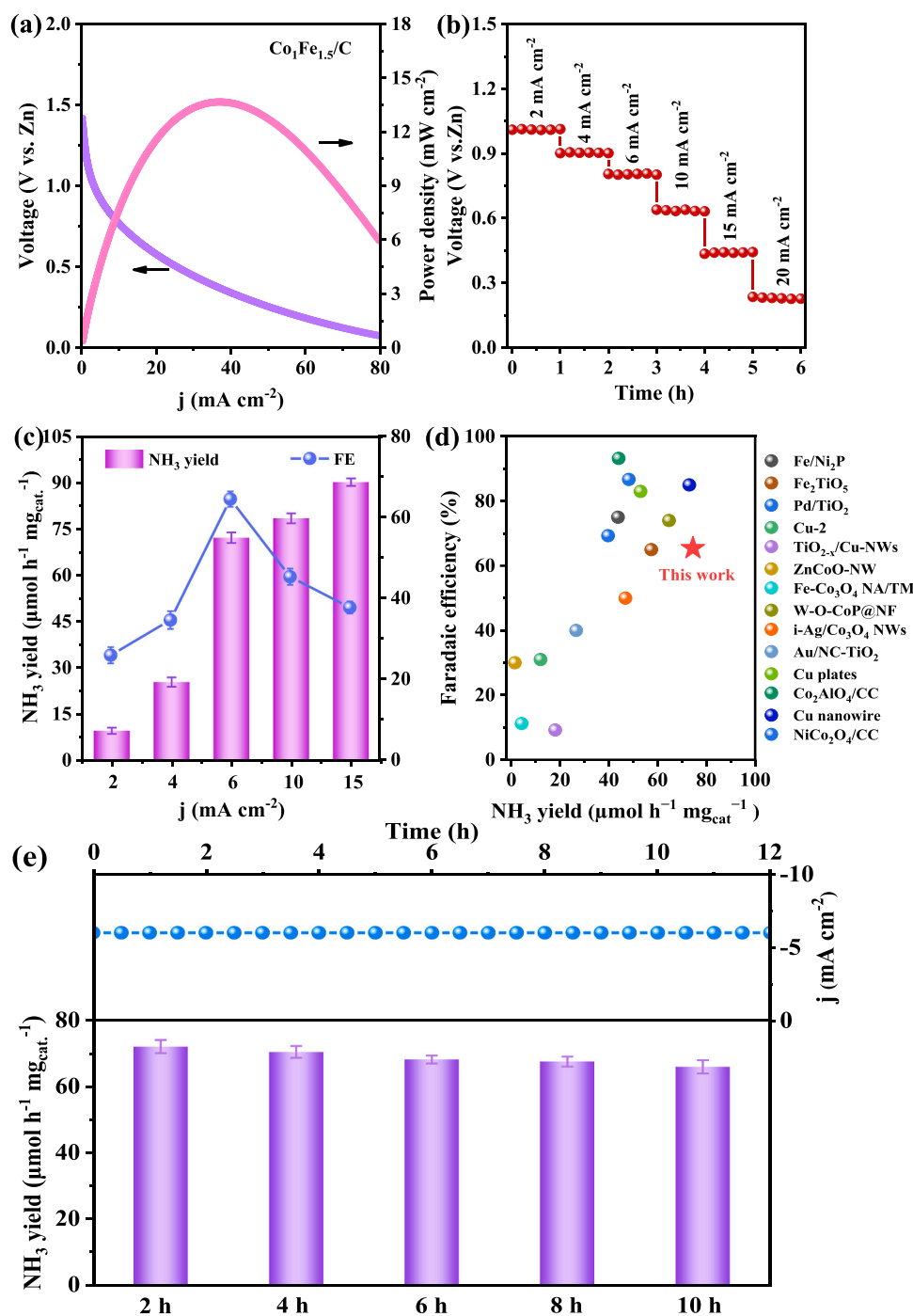


**Fig. 6.** (a) Discharging current-voltage curve of the Zn-NO<sub>3</sub> battery. (b) Voltages corresponding to varying current densities. (c) FE and NH<sub>3</sub> yield at different current densities of the Co<sub>1</sub>Fe<sub>1.5</sub>/C based Zn-NO<sub>3</sub> battery. (d) Comparison of battery performance with other reported catalysts (Supporting information, Ref. 2–15, Table S4). (e) The current density and NH<sub>3</sub> yield variation of the long-term stability test.

substance  $^*\text{NO}$  substance adsorbed on the surface of CoFe[29], which is conducive to the improvement of the catalytic activity of the catalyst. Such an optimization might make the adsorption and activation of  $^*\text{NO}_3$  or  $^*\text{NO}$  over the metal sites be altered, which lowers the energy barrier of the reaction process and accelerates the  $\text{NO}_3$  reaction rate. Based on the preferred  $\text{NO}_3\text{RR}$  reaction pathway reported [11] and the free energy of several key intermediates on Co, Fe, and CoFe alloy models is calculated correspondingly (Fig. 5h). It is noteworthy that regarding the metallic Co model, the first step of the protonation pathway of  $^*\text{NO}$  requires a higher energy barrier input (0.91 eV), while this process becomes spontaneous smoothly onto the Fe or FeCo alloys. The presence of strong competition for hydrogen precipitation in metallic Co, leads to a tendency to form  $^*\text{HH}$  rather than  $^*\text{HNO}$  in the first protonation step. Therefore, a higher energy barrier is required to optimize the reaction orientation. When Fe alloying Co, the introduction of Fe enables this step to occur spontaneously due to its ability to inhibit hydrogen precipitation competition. It can be suggested that the Fe alloying Co suppresses HER by optimizing the electronic structure of the Co site, thus altering the first-step protonation energy barrier of  $\text{NO}_3\text{RR}$  over the Co site. Furthermore,  $^*\text{HNO}$  is sequentially protonated to  $^*\text{H}_2\text{NO}$ ,  $^*\text{H}_3\text{NO}$ ,  $^*\text{NH}_3$ , and  $+\text{NH}_3$ . In particular, the third protonation pathway of  $^*\text{H}_2\text{NO}$  acting as the decisive step is preferred for alloyed CoFe (+0.43 eV) compared to Fe (+0.54 eV). In addition, when Co was overcoming the first protonation step, the subsequent protonation steps all proceeded spontaneously. This also demonstrates the good selectivity of Co towards  $^*\text{NH}_x$ . Interestingly, the  $\text{NH}_3$  desorption energy barrier over CoFe alloy becomes reduced, suggesting  $\text{NH}_3$  desorption becomes more easily, agreeing with the experimental results. The above DFT calculation demonstrates the Fe alloying Co makes the reaction process easier and smoother by suppressing HER, which affects the adsorption and activation of key active species during this relay catalytic process.

Based on the excellent performance of  $\text{Co}_1\text{Fe}_{1.5}/\text{C}$  in  $\text{NO}_3\text{RR}$ , a novel Zn- $\text{NO}_3$  battery was assembled in a neutral environment with a zinc sheet as the anode and  $\text{Co}_1\text{Fe}_{1.5}/\text{C}$  immobilized on a carbon cloth as the cathode. Figure 35 depicts a zinc Nitrate cell with  $\text{Co}_1\text{Fe}_{1.5}/\text{C}$  as the cathode, exhibiting a constant open-circuit potential of 1.24 V with respect to  $\text{Zn}/\text{Zn}^{2+}$ . It can be found that compared with the theoretical open circuit voltage of 1.8 V of zinc Nitrate battery, there is only a 0.58 V difference, which showcases that our assembled zinc Nitrate has an advantage. The power density of the Zn- $\text{NO}_3$  battery achieves a high power of  $13.7 \text{ mW cm}^{-2}$  at 0.4 V vs. Zn (Fig. 6a). In the discharge test, the current densities of 1, 2, 4, 6, 8, 10, and  $12 \text{ mA cm}^{-2}$  could be kept extremely stable for 1 h (Fig. 6b). We find that the gap between the discharge voltage in Fig. 6a and Fig. 6b may be due to the fact that internal resistance of the battery and the polarization phenomenon of Zn- $\text{NO}_3$  battery. Fig. 6c shows the Faraday efficiency and the corresponding  $\text{NH}_3$  yield at different discharge current densities for 1 h. The  $\text{NH}_3$  yield increases with increasing current density, and the Faraday efficiency reaches a maximum at a current density of  $6 \text{ mA cm}^{-2}$ . Remarkably, the  $\text{Co}_1\text{Fe}_{1.5}/\text{C}$ -based battery possesses a higher  $\text{NH}_3$  yield of  $90.1 \mu\text{mol h}^{-1} \text{ mg}_{\text{cat}}^{-1}$  at  $15 \text{ mA cm}^{-2}$  and a maximal Faraday efficiency of 65.4 % at  $6 \text{ mA cm}^{-2}$  (Fig. 6c). The excellent electrochemical durability of the battery was verified by a sustained discharge test (Fig. 6e). We found a slight decrease in the yield of  $\text{NH}_3$  over the long-term stability test. The small decrease in the battery  $\text{NH}_3$  yield could be due to internal Nitrate concentration depletion or zinc flake loss[28], and this phenomenon seems to often exist. In addition, the performance of our catalyst was compared with the advanced catalysts reported in recent years, which can prove that the catalyst has good Faraday efficiency and higher Ammonia yield (Table S4). Thus, the  $\text{Co}_1\text{Fe}_{1.5}/\text{C}$ -based Zn- $\text{NO}_3$  battery has potential as a potential energy conversion device for electrocatalytic Nitrate reduction under ambient conditions.

Since the product ( $\text{NH}_3$ ) is recycled from the electrocatalytic process its utilization is still a concern. Therefore, a sequential  $\text{NO}_3\text{RR}$  and  $\text{NH}_3$  collection system is highly appealed for realizing continuous-flow Nitrate removal and nitrogen recycling. Based on the tactic mentioned by

Hou[50] et al., industrial by-products such as  $\text{NH}_4\text{Cl}/(\text{NH}_4)_2\text{SO}_4$  can be synthesized in a directed manner by introducing the Ammonia solution into the system described separated  $\text{NO}_3\text{-NH}_3$  conversion cell and an  $\text{NH}_3\text{-N}$  collection cell. Specifically, the process involves a conversion of  $\text{NO}_3\text{-N}$  into  $\text{NH}_3\text{-N}$  over the catalysts in the conversion cell, followed by the concentration-difference-driven migration of  $\text{NH}_3\text{-N}$  across a superhydrophobic gas-diffusion membrane into an adjacent  $\text{H}_2\text{SO}_4$  or  $\text{HCl}$  solution. Eventually, the reaction between  $\text{NH}_3$  and  $\text{H}_2\text{SO}_4/\text{HCl}$  would yield  $(\text{NH}_4)_2\text{SO}_4$  or  $\text{NH}_4\text{Cl}$ , which can be recovered by the traditional crystallization approach. (Figure 36).

## 4. Conclusions

In summary, by successive electrospinning and precise heat treatment techniques, we constructed porous carbon fiber encapsulated composition-engineered CoFe nanoalloyed catalysts. We demonstrated that the introduction of Fe to alloy Co with tuning composition fraction caused the 110 lattice expansion and changed the electronic structure of the Co site within nanoalloys, which led to improved electron transfer and the redistribution of the Co surface electrons and effectively enhanced the adsorption of  $\text{NO}_3^-$  and intermediates on the catalyst. Besides, the introduced Fe species could work as the typical activated agent for constructing the porosity of carbon fiber apart from its main role as reactive centers and accelerate the charge transfer during the  $\text{NO}_3\text{RR}$  reaction. The in-situ XPS further validated the key role of the optimized Co center for the adsorption of  $\text{NO}^*$ , which synergizes with the Fe center to enable the entire relay  $\text{NO}_3\text{RR}$ . The Ammonia yield reached  $48.2 \pm 1.2 \text{ mg h}^{-1} \text{ mg}_{\text{cat}}^{-1}$  over  $\text{Co}_1\text{Fe}_{1.5}/\text{C}$  with a Faraday efficiency of  $90.8 \pm 1.5 \%$  at  $-1.1 \text{ V}$  vs. RHE reaction potential, which outperformed the most reported the-state-to-the-art  $\text{NO}_3\text{RR}$  catalysts employed at high reaction potential. In addition, the  $\text{NO}_3\text{RR}$  cycle stability of  $\text{Co}_1\text{Fe}_{1.5}/\text{C}$  during several successive electrolyte replacements is up to 200 h, affording the practical potential. The  $\text{Co}_1\text{Fe}_{1.5}/\text{C}$ -based Zn- $\text{NO}_3$  battery was further constructed as a potential energy conversion device and reached a high power of  $13.7 \text{ mW cm}^{-2}$  at 0.4 V and achieved a high  $\text{NH}_3$  yield of  $72.1 \mu\text{mol h}^{-1} \text{ cm}^{-2}$  at  $15 \text{ mA cm}^{-2}$  and maximal Faraday efficiency of 65.4 % at  $6 \text{ mA cm}^{-2}$ , which shows its potential in the practical multifunctional application.

## CRedit authorship contribution statement

**Enxian Yuan:** Methodology. **Fu Yang:** Writing – review & editing, Supervision, Project administration, Investigation, Funding acquisition, Formal analysis, Data curation, Conceptualization. **Aihua Yuan:** Formal analysis. **Yang Liu:** Writing – original draft, Investigation, Formal analysis, Data curation. **Weidong Shi:** Writing – review & editing. **Xiu Zhong:** Investigation, Formal analysis. **Mengting Liu:** Investigation, Formal analysis. **Yanyun Wang:** Investigation, Formal analysis. **Jun Yang:** Formal analysis. **Fei Gao:** Formal analysis. **Yingguo Li:** Formal analysis. **Hongyao Zhao:** Investigation, Formal analysis. **Zhenxiao Wang:** Formal analysis. **Ruiting Ni:** Formal analysis.

## Declaration of Competing Interest

The authors declare that they have no known competing financial interests or personal relationships that could have appeared to influence the work reported in this paper.

## Data Availability

The authors are unable or have chosen not to specify which data has been used.

## Acknowledgments

The research presented in this paper received financial support from



several sources, including the China National Natural Science Foundation (21908085), the China Postdoctoral Science Foundation (2023M731422), Open project of State Key Laboratory of Materials Chemical Engineering (KL-NICE-23B03), and the Science and Technology Plan School-Enterprise Cooperation Industry-University-Research Forward-looking Project of ZhangjiaGang (ZKYY2341). We gratefully acknowledge the assistance provided by the Instrumental Analysis Center at Jiangsu University of Science and Technology for their contributions to the characterization aspects of this study.

## Appendix A. Supporting information

Supplementary data associated with this article can be found in the online version at [doi:10.1016/j.apcatb.2024.124205](https://doi.org/10.1016/j.apcatb.2024.124205).

## References

- [1] Y. Xu, Y. Wen, T. Ren, H. Yu, K. Deng, Z. Wang, X. Li, L. Wang, H. Wang, Engineering the surface chemical microenvironment over CuO nanowire arrays by polyaniline modification for efficient Ammonia electrosynthesis from Nitrate, *Appl. Catal. B* 320 (2023) 121981, <https://doi.org/10.1016/j.apcatb.2022.121981>.
- [2] J.-C. Liu, X.-L. Ma, Y. Li, Y.-G. Wang, H. Xiao, J. Li, Heterogeneous Fe<sub>3</sub> single-cluster catalyst for Ammonia synthesis via an associative mechanism, *Nat. Commun.* 9 (2018) 1610, <https://doi.org/10.1038/s41467-018-03795-8>.
- [3] S. Li, P. Ma, C. Gao, L. Liu, X. Wang, M. Shakouri, R. Chernikov, K. Wang, D. Liu, R. Ma, J. Wang, Reconstruction-induced NiCu-based catalysts towards paired electrochemical refining, *Energy Environ. Sci.* 15 (2022) 3004–3014, <https://doi.org/10.1039/d2ee00461e>.
- [4] J. Feng, H. Pan, Electronic state optimization for electrochemical N<sub>2</sub> reduction reaction in aqueous solution, *J. Mater. Chem. A* 8 (2020) 13896–13915, <https://doi.org/10.1039/d0ta04709k>.
- [5] J. Liang, Z. Li, L. Zhang, X. He, Y. Luo, D. Zheng, Y. Wang, T. Li, H. Yan, B. Ying, S. Sun, Q. Liu, M.S. Hamdy, B. Tang, X. Sun, Advances in Ammonia electrosynthesis from ambient Nitrate/nitrite reduction, *Chem* 9 (2023) 1768–1827, <https://doi.org/10.1016/j.chempr.2023.05.037>.
- [6] J. Li, Y. Zhang, C. Liu, L.R. Zheng, E. Petit, K. Qi, Y. Zhang, H. Wu, W. Wang, A. Tiberj, X. Wang, M. Chhowalla, L. Lajaunie, R. Yu, D. Voirey, 3.4 % solar-to-Ammonia efficiency from Nitrate using Fe single atomic catalyst supported on MoS<sub>2</sub> nanosheets, *Adv. Funct. Mater.* 32 (2022) 2108316, <https://doi.org/10.1002/adfm.202108316>.
- [7] M. Wang, S. Liu, T. Qian, J. Liul, J. Zhou, H. Ji, J. Xiong, J. Zhong, C. Yan, Over 56.55 % Faradaic efficiency of ambient Ammonia synthesis enabled by positively shifting the reaction potential, *Nat. Commun.* 10 (2019) 341, <https://doi.org/10.1038/s41467-018-08120-x>.
- [8] L. Yue, W. Song, L. Zhang, Y. Luo, Y. Wang, T. Li, B. Ying, S. Sun, D. Zheng, Q. Liu, A. Farouk, M.S. Hamdy, S. Alfaifi, X. Sun, Recent advance in heterogenous electrocatalysts for highly selective nitrite reduction to Ammonia under ambient condition, *Small Struct.* 4 (2023) e2300168, <https://doi.org/10.1002/sstr.202300168>.
- [9] D. Liu, M. Chen, X. Du, H. Ai, K.H. Lo, S. Wang, S. Chen, G. Xing, X. Wang, H. Pan, Development of electrocatalysts for efficient nitrogen reduction reaction under ambient condition, *Adv. Funct. Mater.* 31 (2021) 2008983, <https://doi.org/10.1002/adfm.202008983>.
- [10] W.-J. Sun, H.-Q. Ji, L.-X. Li, H.-Y. Zhang, Z.-K. Wang, J.-H. He, J.-M. Lu, Built-in electric field triggered interfacial accumulation effect for efficient Nitrate removal at ultra-low concentration and electroreduction to Ammonia, *Angew. Chem., Int. Ed.* 60 (2021) 22933–22939, <https://doi.org/10.1002/anie.202109785>.
- [11] S. Ye, Z. Chen, G. Zhang, W. Chen, C. Peng, X. Yang, L. Zheng, Y. Li, X. Ren, H. Cao, D. Xue, J. Qiu, Q. Zhang, J. Liu, Elucidating the activity, mechanism and application of selective electrosynthesis of Ammonia from Nitrate on cobalt phosphide, *Energy Environ. Sci.* 15 (2022) 760–770, <https://doi.org/10.1039/d1ee03097c>.
- [12] G.-F. Chen, Y. Yuan, H. Jiang, S.-Y. Ren, L.-X. Ding, L. Ma, T. Wu, J. Lu, H. Wang, Electrochemical reduction of Nitrate to Ammonia via direct eight-electron transfer using a copper-molecular solid catalyst, *Nat. Energy* 5 (2020) 605–613, <https://doi.org/10.1038/s41560-020-0654-1>.
- [13] Y. Wang, W. Zhou, R. Jia, Y. Yu, B. Zhang, Unveiling the activity origin of a copper-based electrocatalyst for selective Nitrate reduction to Ammonia, *Angew. Chem. Int. Ed.* 59 (2020) 5350–5354, <https://doi.org/10.1002/anie.201915992>.
- [14] W. Song, L. Yue, X. Fan, Y. Luo, B. Ying, S. Sun, D. Zheng, Q. Liu, M.S. Hamdy, X. Sun, Recent progress and strategies on the design of catalysts for electrochemical Ammonia synthesis from Nitrate reduction, *Inorg. Chem. Front.* 10 (2023) 3489–3514, <https://doi.org/10.1039/d3qi00554b>.
- [15] Y. Li, X. Ru, M. Yang, Y. Zheng, S. Yin, C. Hong, F. Peng, M. Qu, C. Xue, J. Lu, L. Fang, C. Su, D. Chen, J. Xu, C. Yan, Z. Li, X. Xu, Z. Shao, Flexible silicon solar cells with high power-to-weight ratios, *Nature* 626 (2024) 105–110, <https://doi.org/10.1038/s41586-023-06948-y>.
- [16] X. Zhong, E. Yuan, F. Yang, Y. Liu, H. Lu, J. Yang, F. Gao, Y. Zhou, J. Pan, J. Zhu, C. Yu, C. Zhu, A. Yuan, E.H. Ang, Optimizing oxygen vacancies through grain boundary engineering to enhance electrocatalytic nitrogen reduction, [e2306673120-e2306673120](https://doi.org/10.1038/s41560-023-00553-0), *Proc. Natl. Acad. Sci. U. S. A.* 120 (2023), <https://doi.org/10.1073/pnas.2306673120>.
- [17] Y. Li, J. Ma, Z. Wu, Z. Wang, Direct electron transfer coordinated by oxygen vacancies boosts selective Nitrate reduction to N<sub>2</sub> on a Co-CuO<sub>2</sub> electroactive filter, *Environ. Sci. Technol.* 56 (2022) 8673–8681, <https://doi.org/10.1021/acs.est.1c05841>.
- [18] T. Zhao, X. Li, J. Hu, J. Zhou, X. Jia, G. Hu, P-doped FeCo<sub>2</sub>O<sub>4</sub> in-situ decorated on carbon cloth as robust electrocatalysts for reducing Nitrate and nitrite to Ammonia, *J. Environ. Chem. Eng.* 11 (2023) 110122, <https://doi.org/10.1016/j.jece.2023.110122>.
- [19] J. Wang, T. Feng, J. Chen, V. Ramalingam, Z. Li, D.M. Kabtamu, J.-H. He, X. Fang, Electrocatalytic Nitrate/nitrite reduction to Ammonia synthesis using metal nanocatalysts and bio-inspired metalloenzymes, *Nano Energy* 86 (2021) 106088, <https://doi.org/10.1016/j.nanoen.2021.106088>.
- [20] L. Qiao, D. Liu, A. Zhu, J. Feng, P. Zhou, C. Liu, K.W. Ng, H. Pan, Nickel-facilitated in-situ surface reconstruction on spinel Co<sub>3</sub>O<sub>4</sub> for enhanced electrochemical Nitrate reduction to Ammonia, *Appl. Catal. B* 340 (2024) 123219, <https://doi.org/10.1016/j.apcatb.2023.123219>.
- [21] G.A. Cerron-Calle, A.S. Fajardo, C.M. Sanchez-Sanchez, S. Garcia-Segura, Highly reactive Cu-Pt bimetallic 3D-electrocatalyst for selective Nitrate reduction to Ammonia, *Appl. Catal. B* 302 (2022) 120844, <https://doi.org/10.1016/j.apcatb.2021.120844>.
- [22] Z.-X. Ge, T.-J. Wang, Y. Ding, S.-B. Yin, F.-M. Li, P. Chen, Y. Chen, Interfacial engineering enhances the electroactivity of frame-like concave RhCu bimetallic nanocubes for Nitrate reduction, *Adv. Energy Mater.* 12 (2022) 2103916, <https://doi.org/10.1002/aenm.202103916>.
- [23] X. Fan, D. Zhao, Z. Deng, L. Zhang, J. Li, Z. Li, S. Sun, Y. Luo, D. Zheng, Y. Wang, B. Ying, J. Zhang, A.A. Alshehri, Y. Lin, C. Tang, X. Sun, Y. Zheng, Constructing Co@TiO<sub>2</sub> nanoarray heterostructure with Schottky contact for selective electrocatalytic Nitrate reduction to Ammonia, *Small* 19 (2023) e2208036, <https://doi.org/10.1002/smll.202208036>.
- [24] W. Wen, P. Yan, W. Sun, Y. Zhou, X.-Y. Yu, Metastable phase Cu with optimized local electronic state for efficient electrocatalytic production of Ammonia from Nitrate, *Adv. Funct. Mater.* 33 (2023) 2212236, <https://doi.org/10.1002/adfm.202212236>.
- [25] Y. Wen, H. Zhu, J. Hao, S. Lu, W. Zong, F. Lai, P. Ma, W. Dong, T. Liu, M. Du, Metal-free boron and sulphur co-doped carbon nanofibers with optimized p-band centers for highly efficient nitrogen electroreduction to Ammonia, *Appl. Catal. B* 292 (2021) 120144, <https://doi.org/10.1016/j.apcatb.2021.120144>.
- [26] X. Fan, C. Liu, Z. Li, Z. Cai, L. Ouyang, Z. Li, X. He, Y. Luo, D. Zheng, S. Sun, Y. Wang, B. Ying, Q. Liu, A. Farouk, M.S.S. Hamdy, F. Gong, X. Sun, Y. Zheng, Pd-doped Co<sub>3</sub>O<sub>4</sub> nanoarray for efficient eight-electron Nitrate electrocatalytic reduction to Ammonia synthesis, *Small* 19 (2023) e202303424, <https://doi.org/10.1002/smll.202303424>.
- [27] W. Gao, K. Xie, J. Xie, X. Wang, H. Zhang, S. Chen, H. Wang, Z. Li, C. Li, Alloying of Cu with Ru enabling the relay catalysis for reduction of Nitrate to Ammonia, *Adv. Mater.* 35 (2023) 2202952, <https://doi.org/10.1002/adma.202202952>.
- [28] J. Xu, S. Zhang, H. Liu, S. Liu, Y. Yuan, Y. Meng, M. Wang, C. Shen, Q. Peng, J. Chen, X. Wang, L. Song, K. Li, W. Chen, Breaking local charge symmetry of iron single atoms for efficient electrocatalytic Nitrate reduction to Ammonia, *Angew. Chem. Int. Ed.* 62 (2023) e202308044, <https://doi.org/10.1002/anie.202308044>.
- [29] X. Zhao, Y. Jiang, M. Wang, S. Liu, Z. Wang, T. Qian, C. Yan, Optimizing Intermediate Adsorption Via Heteroatom Ensemble Effect over RuFe bimetallic alloy for enhanced Nitrate electroreduction to Ammonia, *Adv. Energy Mater.* 13 (2023) 2301409, <https://doi.org/10.1002/aenm.202301409>.
- [30] T. Zhao, J. Zhou, D. Zhang, Y. Wang, S. Zhou, J. Chen, G. Hu, Self-supported P-doped NiFe<sub>2</sub>O<sub>4</sub> micro-sheet arrays for the efficient conversion of nitrite to Ammonia, *J. Colloid Interface Sci.* 650 (2023) 143–150, <https://doi.org/10.1016/j.jcis.2023.06.194>.
- [31] J. Wang, T. Feng, J. Chen, J.H. He, X. Fang, Flexible 2D Cu metal: organic framework@MXene film electrode with excellent durability for highly selective electrocatalytic NH<sub>3</sub> synthesis, *Research* 2022 (2022) 9837012, <https://doi.org/10.34133/2022/9837012>.
- [32] J. Hu, T. Zhao, H. Zhang, X. Li, A. Shi, X. Li, Q. Wang, G. Hu, Fe<sub>2</sub>P nanoparticle-decorated porous biochar for high-efficiency electrosynthesis of Ammonia from toxic nitrite, *Surf. Interfaces* 38 (2023) 102818, <https://doi.org/10.1016/j.surf.2023.102818>.
- [33] L. Ying, S. Sun, W. Liu, H. Zhu, Z. Zhu, A. Liu, L. Yang, S. Lu, F. Duan, C. Yang, M. Du, Heterointerface engineering in bimetal alloy/metal carbide for evolution reaction, *Renew. Energy* 161 (2020) 1036–1045, <https://doi.org/10.1016/j.renene.2020.07.150>.
- [34] G. Chen, R. Gao, Y. Zhao, Z. Li, G.I.N. Waterhouse, R. Shi, J. Zhao, M. Zhang, L. Shang, G. Sheng, X. Zhang, X. Wen, L.-Z. Wu, C.-H. Tung, T. Zhang, Alumina-supported CoFe alloy catalysts derived from layered-double-hydroxide nanosheets for efficient photothermal CO<sub>2</sub> hydrogenation to hydrocarbons, *Adv. Mater.* 30 (2018) 1704663, <https://doi.org/10.1002/adma.201704663>.
- [35] J. Hao, H. Zhu, Y. Li, P. Liu, S. Lu, F. Duan, W. Dong, Y. Lu, T. Liu, M. Du, Tuning the electronic structure of AuNi homogeneous solid-solution alloy with positively charged Ni center for highly selective electrochemical CO<sub>2</sub> reduction, *Chem. Eng. J.* 404 (2021) 126523, <https://doi.org/10.1016/j.cej.2020.126523>.
- [36] M. Chen, K. Chang, Y. Zhang, Z. Zhang, Y. Dong, X. Qiu, H. Jiang, Y. Zhu, J. Zhu, Cation-radius-controlled Sn-O bond length boosting CO<sub>2</sub> electroreduction over Sn-Based perovskite oxides, *Angew. Chem. Int. Ed.* 62 (2023) e2305530, <https://doi.org/10.1002/anie.202305530>.
- [37] X. Liu, H. Jang, P. Li, J. Wang, Q. Qin, M.G. Kim, G. Li, J. Cho, Antimony-Based composites loaded on phosphorus-doped carbon for boosting faradaic efficiency of

- the electrochemical nitrogen reduction reaction, *Angew. Chem., Int. Ed.* 58 (2019) 13329–13334, <https://doi.org/10.1002/anie.201906521>.
- [38] S. Wu, Y. Jiang, W. Luo, P. Xu, L. Huang, Y. Du, H. Wang, X. Zhou, Y. Ge, J. Qian, H. Nie, Z. Yang, Ag-Co<sub>3</sub>O<sub>4</sub>-CoOOH-nanowires tandem catalyst for efficient electrocatalytic conversion of Nitrate to Ammonia at low overpotential via triple reactions, *Adv. Sci.* 10 (2023) 2303789, <https://doi.org/10.1002/adv.202303789>.
- [39] N. Zhang, G. Zhang, P. Shen, H. Zhang, D. Ma, K. Chu, Lewis acid Fe-V pairs promote Nitrate electroreduction to Ammonia, *Adv. Funct. Mater.* 33 (2023) 2211537, <https://doi.org/10.1002/adfm.202211537>.
- [40] X. Zi, J. Wan, X. Yang, W. Tian, H. Zhang, Y. Wang, Vacancy-rich 1T-MoS<sub>2</sub> monolayer confined to MoO<sub>3</sub> matrix: an interface-engineered hybrid for efficiently electrocatalytic conversion of nitrogen to Ammonia, *Appl. Catal. B* 286 (2021) 119870, <https://doi.org/10.1016/j.apcatb.2020.119870>.
- [41] M. Testa-Anta, B. Rivas-Murias, V. Salgueirino, Spin frustration drives exchange bias sign crossover in CoFe<sub>2</sub>O<sub>4</sub>-Cr<sub>2</sub>O<sub>3</sub> nanocomposites, *Adv. Funct. Mater.* 29 (2019) 1900030, <https://doi.org/10.1002/adfm.201900030>.
- [42] J. Wang, J. Tang, B. Ding, V. Malgras, Z. Chang, X. Hao, Y. Wang, H. Dou, X. Zhang, Y. Yamauchi, Hierarchical porous carbons with layer-by-layer motif architectures from confined soft-template self-assembly in layered materials, *Nat. Commun.* 8 (2017) 15717, <https://doi.org/10.1038/ncomms15717>.
- [43] R. Wang, X.-Y. Dong, J. Du, J.-Y. Zhao, S.-Q. Zang, MOF-derived bifunctional Cu<sub>3</sub>P nanoparticles coated by a N,P-codoped carbon shell for hydrogen evolution and oxygen reduction, *Adv. Mater.* 30 (2018) 1703711, <https://doi.org/10.1002/adma.201703711>.
- [44] R. Boppella, M.P. Austeria, Y. Kim, E. Kim, I. Song, Y. Eom, D.P. Kumar, M. Balamurugan, E. Sim, D.H. Kim, T.K. Kim, Pyrrolic N-stabilized monovalent Ni single-atom electrocatalyst for efficient CO<sub>2</sub> reduction: identifying the role of Pyrrolic-N and synergistic electrocatalysis, *Adv. Funct. Mater.* 32 (2022) 2202351, <https://doi.org/10.1002/adfm.202202351>.
- [45] X. Deng, Y. Yang, L. Wang, X.-Z. Fu, J.-L. Luo, Metallic Co nanoarray catalyzes selective NH<sub>3</sub> production from electrochemical Nitrate reduction at current densities exceeding 2 A cm<sup>-2</sup>, *Adv. Sci.* 8 (2021) 2004523, <https://doi.org/10.1002/adv.202004523>.
- [46] Z. Fang, Z. Jin, S. Tang, P. Li, P. Wu, G. Yu, Porous two-dimensional iron-cyano nanosheets for high-rate electrochemical Nitrate reduction, *ACS Nano* 16 (2022) 1072–1081, <https://doi.org/10.1021/acsnano.1c08814>.
- [47] R. Zhao, Q. Yan, L. Yu, T. Yan, X. Zhu, Z. Zhao, L. Liu, J. Xi, A Bi-Co corridor construction effectively improving the selectivity of electrocatalytic Nitrate reduction toward Ammonia by nearly 100 %, *Adv. Mater.* 35 (2023) 2306633, <https://doi.org/10.1002/adma.202306633>.
- [48] Y. Wang, A. Xu, Z. Wang, L. Huang, J. Li, F. Li, J. Wicks, M. Luo, D.-H. Nam, C.-S. Tan, Y. Ding, J. Wu, Y. Lum, D. Cao-Thang, D. Sinton, G. Zheng, E.H. Sargent, Enhanced Nitrate-to-Ammonia activity on Copper-Nickel alloys via tuning of intermediate adsorption, *J. Am. Chem. Soc.* 142 (2020) 5702–5708, <https://doi.org/10.1021/jacs.9b13347>.
- [49] S. Han, H. Li, T. Li, F. Chen, R. Yang, Y. Yu, B. Zhang, Ultralow overpotential Nitrate reduction to Ammonia via a three-step relay mechanism, *Nat. Catal.* 6 (2023) 402–414, <https://doi.org/10.1038/s41929-023-00951-2>.
- [50] Z. Liu, F. Shen, L. Shi, Q. Tong, M. Tang, Y. Li, M. Peng, Z. Jiao, Y. Jiang, L. Ao, W. Fu, X. Lv, G. Jiang, L. Hou, Electronic structure optimization and proton-transfer enhancement on titanium oxide-supported copper nanoparticles for enhanced nitrogen recycling from Nitrate-contaminated water, *Environ. Sci. Technol.* 57 (2023) 10117–10126, <https://doi.org/10.1021/acs.est.3c03431>.